© 2020. Published by The Company of Biologists Ltd | Development (2020) 147, dev186312. doi:10.1242/dev.186312

RESEARCH ARTICLE

Developmental arrest of *Drosophila* larvae elicits presynaptic depression and enables prolonged studies of neurodegeneration

Sarah Perry[1,*], Pragya Goel[1,*], Nancy L. Tran[1], Cristian Pinales[2], Christopher Buser[2], Daniel L. Miller[3,4], Barry Ganetzky[3] and Dion Dickman[1,‡]

ABSTRACT

Synapses exhibit an astonishing degree of adaptive plasticity in healthy and disease states. We have investigated whether synapses also adjust to life stages imposed by novel developmental programs for which they were never molded by evolution. Under conditions in which *Drosophila* larvae are terminally arrested, we have characterized synaptic growth, structure and function at the neuromuscular junction (NMJ). Although wild-type larvae transition to pupae after 5 days, arrested third instar (ATI) larvae persist for 35 days, during which time NMJs exhibit extensive overgrowth in muscle size, presynaptic release sites and postsynaptic glutamate receptors. Remarkably, despite this exuberant growth, stable neurotransmission is maintained throughout the ATI lifespan through a potent homeostatic reduction in presynaptic neurotransmitter release. Arrest of the larval stage in *stathmin* mutants also reveals a degree of progressive instability and neurodegeneration that was not apparent during the typical larval period. Hence, an adaptive form of presynaptic depression stabilizes neurotransmission during an extended developmental period of unconstrained synaptic growth. More generally, the ATI manipulation provides a powerful system for studying neurodegeneration and plasticity across prolonged developmental timescales.

KEY WORDS: Homeostasis, Synapse, Neurotransmission, *Drosophila*, Plasticity, Neurodegeneration

INTRODUCTION

Synapses are confronted with extensive challenges during development, maturation and aging, yet maintain stable information exchange. The dynamic and at times massive changes in synapse growth, pruning and remodeling, coupled with intrinsic adjustments in neuronal excitability, can lead to unstable physiological activity. The resulting imbalances in excitation and inhibition would propagate within neural circuits to undermine network stability. To adapt to such challenges, synapses are endowed with the capacity to homeostatically adjust neurotransmission while still permitting the flexibility necessary for Hebbian forms of plasticity (Pozo and Goda, 2010; Turrigiano, 2012). The homeostatic control of neural activity operates throughout the organismal lifespan to balance the tension between stability and flexibility, and is thought to break down in neurological and psychiatric diseases (Li et al., 2019; Nelson and Valakh, 2015; Wondolowski and Dickman, 2013). Although it is clear synapses have the capacity to express both Hebbian and homeostatic forms of plasticity, how these processes are integrated and balanced, particularly during development and aging, remain enigmatic.

The *Drosophila* larval neuromuscular junction (NMJ) is an accessible and versatile model for studying synaptic function, plasticity and disease. This model glutamatergic synapse has enabled fundamental insights into synaptic growth, transmission, homeostatic plasticity and injury (Frank et al., 2020; Menon et al., 2013). However, studies in this system are limited by the relatively short larval period of 3-4 days before pupariation, when NMJ accessibility is lost. This short temporal window limits the use of the third instar larval NMJ as a model for interrogating dynamic processes over chronic timescales. Intriguingly, recent studies on the signaling cascades in *Drosophila* that control the transition from third instar to the pupal stage have revealed attractive targets for extending the duration of the third instar stage (Gibbens et al., 2011; Rewitz et al., 2009; Walkiewicz and Stern, 2009).

Developmental progression in *Drosophila* larvae is coordinated through two semi-redundant signaling pathways via Torso and insulin-like receptors that ultimately lead to ecdysone synthesis and release from the prothoracic gland (PG) to drive the transition from the larval stage to pupation (Rewitz et al., 2009; Walkiewicz and Stern, 2009; Yamanaka et al., 2013). A previous study reduced signaling through one arm of this pathway to extend the third instar stage from 5 to 9 days, from which the important observation that NMJs continue to grow and function throughout this period was made (Miller et al., 2012). More recent work has demonstrated that loss of key transcription factors in the PG, including Smox (also known as dSMAD2), can disrupt both signaling pathways to fully arrest larval development and prevent the transition to pupal stages (Gibbens et al., 2011; Ohhara et al., 2017). Remarkably, these arrested third instars (ATI) remain in the larval stage until death. The development of ATI larvae now provides an opportunity to characterize synaptic growth, function and plasticity in a system of terminally persistent expansion beyond normal physiological ranges and has the potential to reveal new insights into processes such as neurodegeneration.

Here, we have developed an optimized approach to arrest *Drosophila* larvae at third instar stages to characterize NMJ growth, function and plasticity. We find that ATI larvae continue to grow and survive for up to 35 days, during which NMJs exhibit exuberant expansion in both pre- and postsynaptic compartments. Interestingly, although this growth should enhance synaptic strength, no significant change is observed compared with

[1]Department of Neurobiology, University of Southern California, Los Angeles, CA 90089, USA. [2]Oak Crest Institute of Science, Monrovia, CA 91016, USA. [3]Laboratory of Genetics, University of Wisconsin, Madison, WI 53706, USA. [4]National Institute of Neurological Disease and Stroke, NIH, Bethesda, MD 20824, USA.
*These authors contributed equally to this work

‡Author for correspondence (dickman@usc.edu)

P.G., 0000-0002-6348-4909; N.L.T., 0000-0001-9382-3847; C.P., 0000-0002-0826-5308; C.B., 0000-0002-4379-3878; B.G., 0000-0001-5418-7577; D.D., 0000-0003-1884-284X

Handling Editor: François Guillemot
Received 13 November 2019; Accepted 18 April 2020

Development (2020) 147, dev186312. doi:10.1242/dev.186312

baseline values. Instead, a potent reduction in presynaptic neurotransmitter release maintains stable synaptic strength across the life of an ATI larva. Finally, the ATI larvae enabled new insights into the progression of neurodegeneration in *stathmin* mutants. Together, arresting larval development now provides a powerful foundation to probe the mechanisms of synaptic growth, function, homeostatic plasticity and neurodegeneration at a model glutamatergic synapse in a genetically tractable system.

RESULTS

Synaptic strength is maintained throughout the lifespan of an ATI larva

To arrest larval development at the third instar stage, we targeted genes that could either disrupt both Torso and insulin signaling pathways or broadly inhibit the synthesis of ecdysone synthesis in the PG, processes ultimately necessary for the transition to pupal stages (Fig. 1A; Gibbens et al., 2011; Ohhara et al., 2017). We reasoned that, if we could prevent the release of ecdysone from the PG by knocking down a key transcript(s), pupation would be delayed indefinitely (Yamanaka et al., 2013). Importantly, knock down of gene expression was restricted to the PG by expression with *phm-Gal4* (Ono et al., 2006), minimizing secondary effects from possible functions in other tissues. We screened several lines described by other investigators that prevent larval transitions to pupariation (Danielsen et al., 2016) and found that a particular RNAi line targeting *smox* was the most effective, reliably preventing pupation in nearly all animals (Fig. 1A,B). *smox* encodes a transcription factor that is required for expression of both *torso* and insulin receptor genes in the PG (Gibbens et al., 2011), as well as having functions in a variety of other tissues (Brummel et al., 1999; Hevia et al., 2017). These persist as ATI larvae and live up to 35 days after egg lay (AEL). Typical wild-type

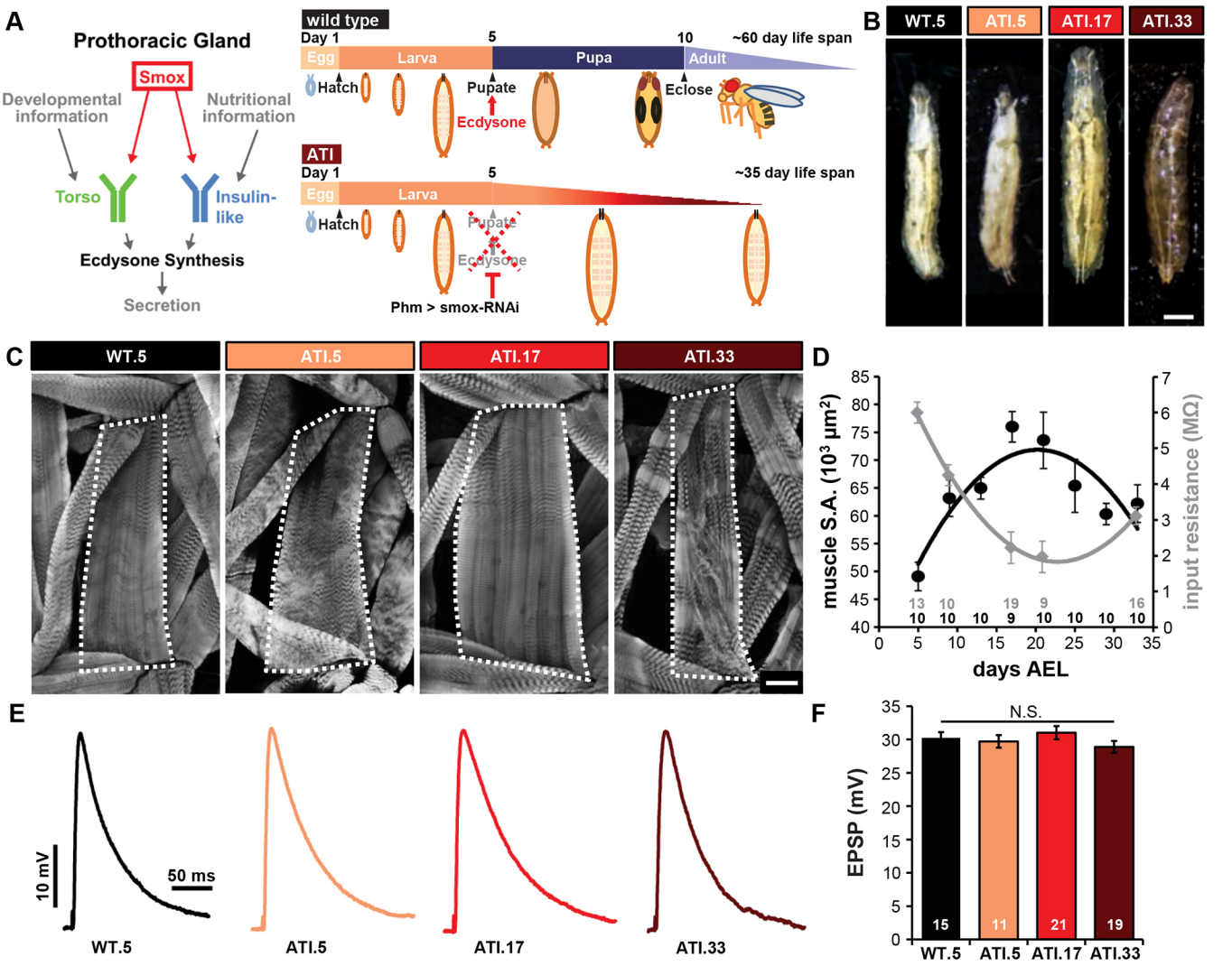

Fig. 1. Synaptic strength remains stable throughout the life of an ATI larva. (A) (Left) Schematic illustrating the signaling pathway that stimulates ecdysone synthesis in the prothoracic gland before pupal formation. The transcription factor Smox is required for the expression of both Torso and insulin receptors. (Right) Schematic comparing wild-type developmental timing and arrested maturation induced by *smox-RNAi*. (B) Representative images of wild-type third instar larvae (WT.5) and *smox-RNAi* (ATI) larvae at different time points (5, 17 and 33 days AEL). Scale bar: 0.5 mm. (C) Representative images of larval body walls stained with anti-phalloidin to highlight muscle structure. M4 surface area is outlined in each image (dotted line). Scale bar: 50 µm. (D) Graph summarizing muscle surface area measurements (black) and muscle input resistance (gray) across the ATI lifespan. (E) Representative EPSP traces for WT.5, ATI.5, ATI.17 and ATI.33 NMJs. (F) Average EPSP amplitudes for the genotypes shown in E. The sample size for each dataset is indicated below the data point (D) or in each bar (E). Error bars indicate ±s.e.m. One-way ANOVA test was performed, followed by a Tukey's multiple-comparison test. N.S., not significant (P>0.05). Detailed statistical information is shown in Table S1.

Development (2020) 147, dev186312. doi:10.1242/dev.186312

larvae spend ∼3 days in the third instar stage before pupation and metamorphosis, living beyond 60 days AEL as adults (Rewitz et al., 2009). For the first 5 days of development, ATI larvae appear to be largely unchanged compared with wild type, but they fail to progress to become 'wandering' third instars. Rather, they continue to feed and gain body mass, peaking at ∼17 days AEL (ATI.17) and then gradually losing body mass until dying soon after 33 days AEL (ATI.33) (Fig. 1B). For further experiments, we compared wild-type larvae at 5 days AEL (WT.5) to ATI larvae at varying time points, including 5 days AEL (ATI.5), a time point similar to wild type; ATI.17, a time corresponding to peak body mass; and ATI.33, a time near the terminal stage of the ATI lifespan.

To investigate NMJs across the ATI lifespan, we first characterized muscle size and passive electrical properties of the muscle. We observed a progressive gain in muscle size across the ATI lifespan, with muscle surface area increasing by over 50%, peaking at ATI.17 and then decreasing to ATI.33 (Fig. 1C,D). Consistent with this substantial increase in muscle size, electrophysiological recordings of NMJs across the ATI lifespan revealed a massive decrease in input resistance, peaking ∼ATI.17 (Fig. 1D). Remarkably, despite these changes in muscle size, synaptic strength [measured by excitatory postsynaptic potential (EPSP) amplitude] remains constant across ATI NMJs (Fig. 1E,F). Thus, as larvae grow and decline through an ATI lifespan, synaptic strength at the NMJ remains constant.

Presynaptic compartments at the NMJ progressively expand in ATI larvae

Clearly, ATI NMJs maintain synaptic strength despite the substantial increase in muscle size that progresses through arrested larval development. In principle, modulations to the number of presynaptic release sites (N), the probability of release at each individual release site (P_r), and/or the postsynaptic response to glutamate release from single synaptic vesicles (quantal size, Q) could stabilize synaptic strength at these NMJs (Dittman and Ryan, 2019). We first assessed synaptic growth to determine whether the number of presynaptic release sites increases in proportion to the muscle surface area. During the conventional 3-4 day period of larval development, there is a 100-fold expansion in the NMJ, with changes to the passive electrical properties of the muscle and a concomitant growth of pre- and postsynaptic compartments (Atwood et al., 1993; Menon et al., 2013; Schuster et al., 1996). These changes are thought to scale NMJ function in parallel with growth and maintain sufficient depolarization for muscle contraction (Davis and Goodman, 1998). However, the progressive increase in muscle size at ATI NMJs poses a further challenge, in which synapses may need to expand to compensate for overgrowth. We therefore considered whether adaptive changes in the growth of motor terminals and/or number of synapses served to stabilize synaptic strength (EPSP amplitude). Using immunostaining, we instead found a progressive enhancement in the neuronal membrane surface area and in the number of boutons per NMJ throughout the ATI lifespan (Fig. 2A-D). In fact, the bouton to muscle area ratio even overshoots the scaling that is normally observed at conventional development between first and third instar larval stages [WT.5: 40 boutons/40,000 μm^2 ratio (Schuster et al., 1996); ATI.17: 100 boutons/75,000 μm^2 ratio; Table S2]. Hence, motor neuron terminals grow in excess to muscle growth.

As NMJ boutons expand across ATI stages, we considered the possibility of a compensatory reduction in the anatomical number of release sites. There is precedence for a reduction in the density of active zones (AZs), independent of NMJ growth, to maintain synaptic strength (Goel et al., 2019b; Graf et al., 2009). To identify individual presynaptic release sites, we immunostained NMJs with an antibody against Bruchpilot (BRP), a central scaffolding protein that constitutes the 'T-bar' structure at AZs in *Drosophila* (Kittel et al., 2006). As ∼96% of release sites are labeled by BRP at the fly NMJ (Akbergenova et al., 2018; Gratz et al., 2019; Wagh et al., 2006), we defined an anatomical release site as a BRP punctum and quantified these structures across the ATI lifespan. Interestingly, we found no significant changes in BRP puncta density across ATI stages, with total BRP puncta number per NMJ increasing in proportion to neuronal membrane area and bouton number (Fig. 2A-D; Table S2). Finally, although the number of BRP puncta increased, the size and fluorescence intensity of these puncta can be reduced at NMJs to compensate for synaptic overgrowth, reducing P_r at individual release sites and maintaining overall synaptic strength (Goel et al., 2019a; 2019b). However, although BRP number at ATI NMJs increases to over threefold that of wild-type NMJs, no compensatory reduction in size and/or intensity of BRP puncta was observed (Fig. 2A, lower panel; Table S2). Indeed, BRP puncta intensity was significantly increased compared with WT.5 levels (Table S2), which may reflect the age-dependent increase in size and intensity and active zones documented at the fly NMJ (Akbergenova et al., 2018). Thus, this anatomical analysis reveals an increase in N at ATI NMJs, implying that other adaptations compensate for excessive growth in ATI larvae.

Postsynaptic receptor fields accumulate at the NMJ over the ATI lifespan

Given the substantial increase in AZ number and intensity but stable synaptic strength, we next considered the possibility that a reduction in Q may have offset the observed presynaptic overgrowth at ATI NMJs. For example, a reduction in the abundance, composition and/or function of postsynaptic glutamate receptors (GluRs) may have occurred at ATI NMJs. At the fly NMJ, two receptor subtypes containing either GluRIIA or GluRIIB subunits form complexes with the essential GluRIIC, GluRIID and GluRIIE subunits to mediate the postsynaptic currents driving neurotransmission (Qin et al., 2005). GluRIIA-containing receptors mediate larger current amplitudes and slower decay kinetics compared with the GluRIIB-containing receptor counterparts (Han et al., 2015; Petersen et al., 1997). We examined the postsynaptic GluRs using antibodies that specifically recognize the GluRIIA or GluRIIB subunits, as well as the common GluRIID subunit (Fig. 3A). Consistent with presynaptic overgrowth, total GluR puncta numbers per NMJ mirrored the increase in presynaptic AZ number (Fig. 3B). Similarly, we observed a significant increase in the abundance of all GluR subunits assessed at ATI NMJs revealed by enhanced fluorescence intensity (Fig. 3C). Together, this demonstrates that postsynaptic receptor fields progressively expand in number and abundance, mirroring the accumulation in presynaptic structures across the ATI lifespan.

We next considered whether an apparent reduction in GluR functionality compensated for the expansion of glutamate receptor fields at ATI NMJs. We determined GluR functionality by electrophysiologically recording miniature events at ATI NMJs. Consistent with the increased fluorescence intensity of all subunits, we observed an ∼50% increase in miniature (m) EPSP amplitude compared with wild-type levels in ATI.17 larvae, an enhancement that persisted through ATI.33 (Fig. 3D,E). Consistent with increased presynaptic growth, we also observed an increase in mEPSP frequency (Fig. 3F). Along with the imaging data suggesting there is

Development (2020) 147, dev186312. doi:10.1242/dev.186312

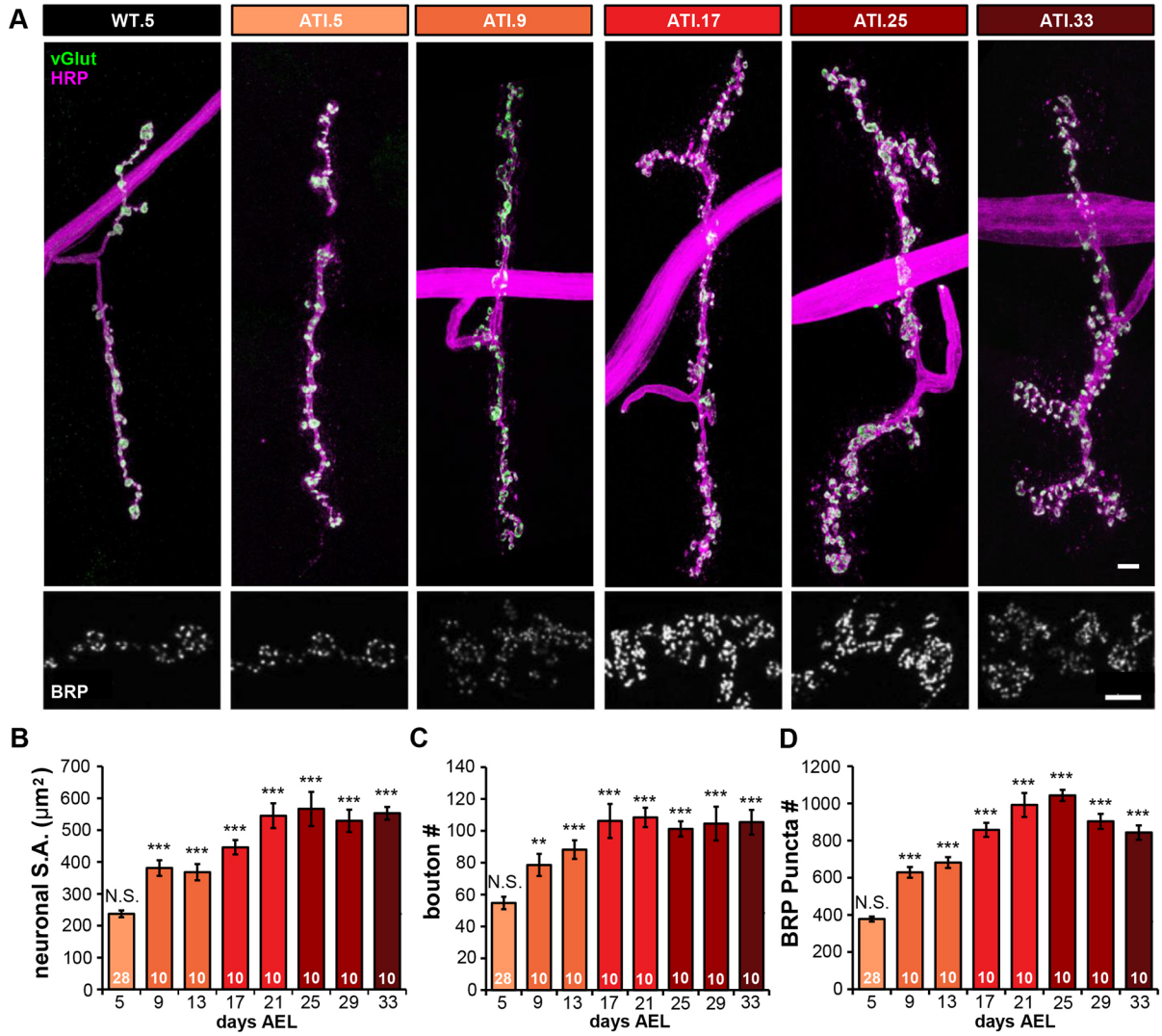

Fig. 2. Progressive synaptic growth and a concomitant accumulation of release sites at ATI NMJs. (A) (Top) Representative images of M4 NMJs at WT.5 and several ATI time points stained with anti-vGlut (synaptic vesicle marker; green) and anti-HRP (neuronal membrane; magenta). (Bottom) Representative portion of the synapses above marked with anti-BRP (active zone marker; white). Scale bars: 10 µm (top); 5 µm (bottom). (B-D) Graphs showing the average neuronal membrane surface area (B), bouton number (C) and BRP puncta number (D) per M4 NMJ for WT.5 and the indicated ATI time points. The sample size for each dataset is indicated in each bar. Error bars indicate ±s.e.m. One-way ANOVA test was performed, followed by a Tukey's multiple-comparison test. $^{**}P \leq 0.01$; $^{***}P \leq 0.001$; N.S., not significant ($P > 0.05$). Detailed statistical information is shown in Table S2.

no change in GluR subunit stoichiometry, we observed no difference in mEPSP decay time constants (Fig. 3G). Thus, both imaging and electrophysiological data indicate that postsynaptic GluR abundance increases concurrently with presynaptic overgrowth at ATI NMJs.

In principle, it is possible that a change in the size of synaptic vesicles at ATI NMJs could also contribute to the enhanced quantal size observed at ATI NMJs. We therefore quantified synaptic vesicle diameter at NMJs of WT and ATI using electron microscopy (Fig. 4A). We observed no significant difference in the average vesicle diameter at NMJs of ATI compared with wild type (Fig. 4B). Therefore, the enhanced mEPSP amplitudes of ATI NMJs are due to an increase in postsynaptic GluR abundance, and yet synaptic strength remains stable across the ATI lifespan. This suggests a homeostatic adjustment in P_r is elicited at ATI NMJs that counteracts both the increased N and enhanced Q. It is unlikely that a retrograde signal from the muscle served to induce this reduction in P_r, as increased expression of postsynaptic GluRs at the fly NMJ similarly enhances mEPSP amplitude but does not alter presynaptic neurotransmitter release (Li et al., 2018c; Petersen et al., 1997). Thus, a reduction in P_r of sufficient magnitude must be induced at ATI NMJs to fully counteract the increase in N and Q to maintain stable synaptic strength.

Synaptic strength at ATI NMJs is maintained through a potent homeostatic decrease in release probability

ATI larvae exhibit exuberant synaptic growth, with accumulations of both pre- and postsynaptic components, resulting in an increased N and Q, factors that should enhance synaptic strength. However, EPSP amplitudes remain stable across the ATI lifespan, implying that P_r must be substantially and precisely diminished to compensate. To further test this idea, we calculated quantal content (the number of synaptic vesicles released per stimulus) and found a substantial reduction at ATI NMJs (Fig. 5A). Next, we assessed presynaptic function independently of mEPSP amplitude by performing failure analysis, where repeated stimulations in low

Development (2020) 147, dev186312. doi:10.1242/dev.186312

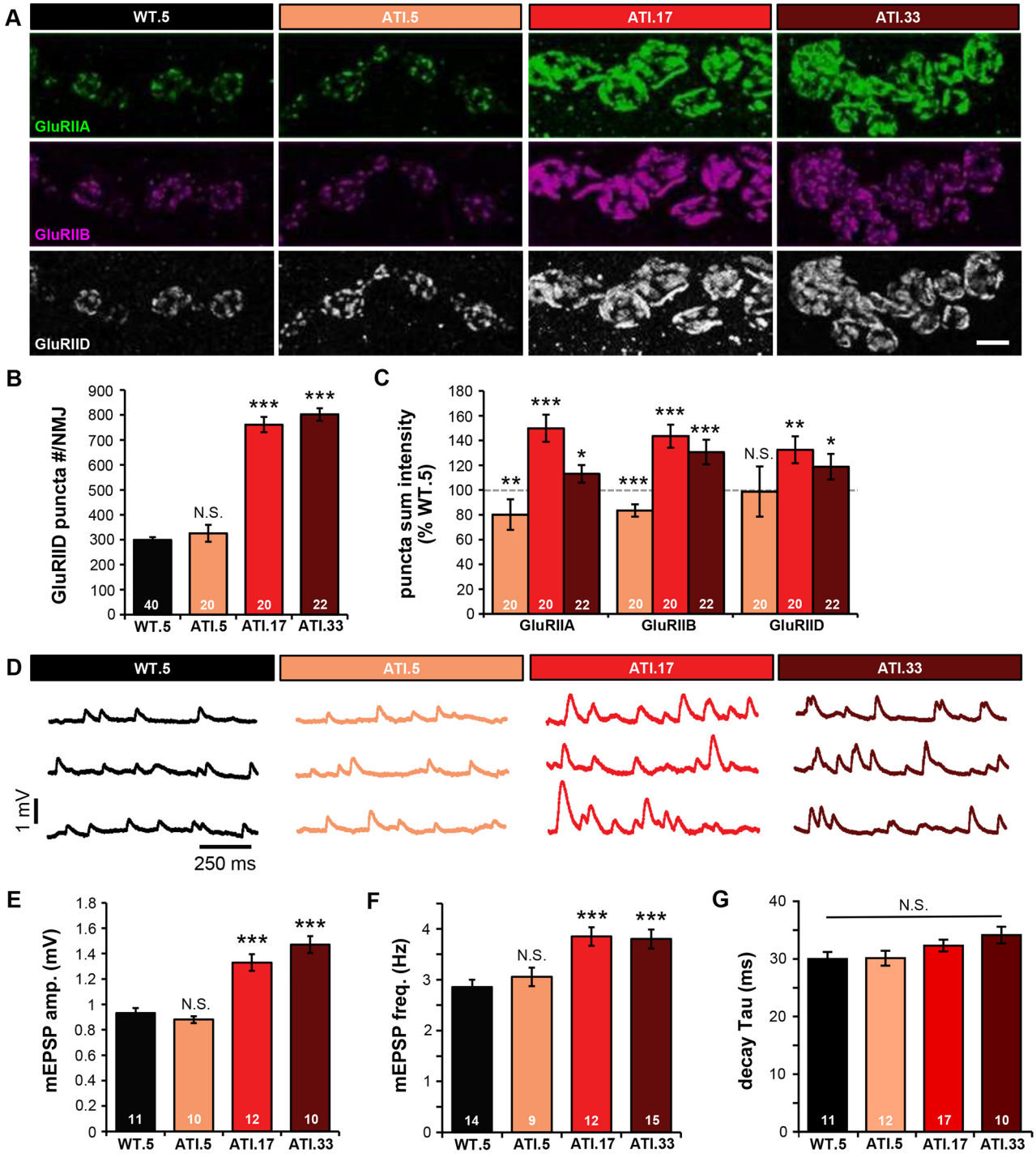

Fig. 3. Postsynaptic glutamate receptors accumulate and quantal size increases over the ATI lifespan. (A) Representative images of the indicated GluR subunit staining at NMJ terminals of M4 in wild type (WT.5) and the indicated ATI time points. Scale bar: 5 µm. (B,C) Quantification of GluRIID puncta number per NMJ (B) and GluR puncta sum fluorescence intensity (C) in the indicated genotypes. The value for wild type at day 5 in C is shown by a dashed line (WT.5, *n*=40). (D) Representative mEPSP traces of WT.5 and the indicated ATI time points. (E-G) Quantification of mEPSP amplitude (E), mEPSP frequency (F) and decay time constant (G) in the indicated genotypes. The sample size for each dataset is indicated in each bar. Error bars indicate ±s.e.m. Two-tailed Student's *t*-test was performed. **P*≤0.05; ***P*≤0.01; ****P*≤0.001; N.S., not significant (*P*>0.05). Detailed statistical information is shown in Table S3.

extracellular Ca^{2+} (0.15 mM) fail to elicit a response in ∼50% of trials in wild type. At ATI NMJs, the failure rate was markedly increased (Fig. 5B), consistent with reduced quantal content. Finally, we assayed paired-pulse ratios to gauge P_r. At low extracellular Ca^{2+} (0.3 mM), paired-pulse facilitation (PPF) is observed at wild-type NMJs, whereas paired-pulse depression (PPD) is found in elevated Ca^{2+} (1.5 mM) (Böhme et al., 2016; Li et al., 2018c). In ATI.17 and ATI.33 NMJs, PPF was significantly increased, whereas PPD was reduced, consistent with reduced P_r relative to wild type (Fig. 5C,D). It is interesting to note that a similar phenomenon has been observed at the *Drosophila* NMJ in the context of typical larval development, referred to as presynaptic

Development (2020) 147, dev186312. doi:10.1242/dev.186312

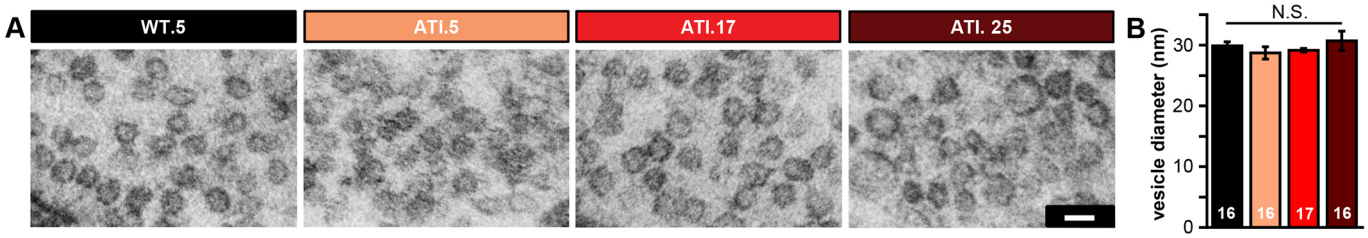

Fig. 4. Synaptic vesicle size remains unchanged across the ATI lifespan. (A) Representative electron micrographs of synaptic vesicles at NMJ terminals of wild-type (WT.5) and ATI larvae at the indicated time points. Scale bar: 50 nm. (B) Quantification of synaptic vesicle diameter in the indicated genotypes reveals no significant differences. The sample size for each dataset is indicated in each bar (samples were obtained from three different animals for each dataset). Error bars indicate ±s.e.m. One-way ANOVA test was performed, followed by a Tukey's multiple-comparison test. N.S., not significant (P>0.05). Detailed statistical information is shown in Table S4.

homeostatic depression (PHD). Here, mEPSP size is enhanced while quantal content is reduced to maintain normal EPSP amplitudes (Daniels et al., 2004; Gaviño et al., 2015; Li et al., 2018c). Although it is not clear that the mechanism of depression is shared between later ATI time points and PHD, we can posit that a homeostatic reduction in presynaptic release probability compensates for increased quantal size to maintain synaptic strength across the ATI life span.

It has previously been shown that NMJs expressing PHD can also express other forms of homeostatic plasticity, including a process referred to as presynaptic homeostatic potentiation (PHP) (Gaviño et al., 2015; Goel et al., 2019a; Li et al., 2018b). To induce PHP, we

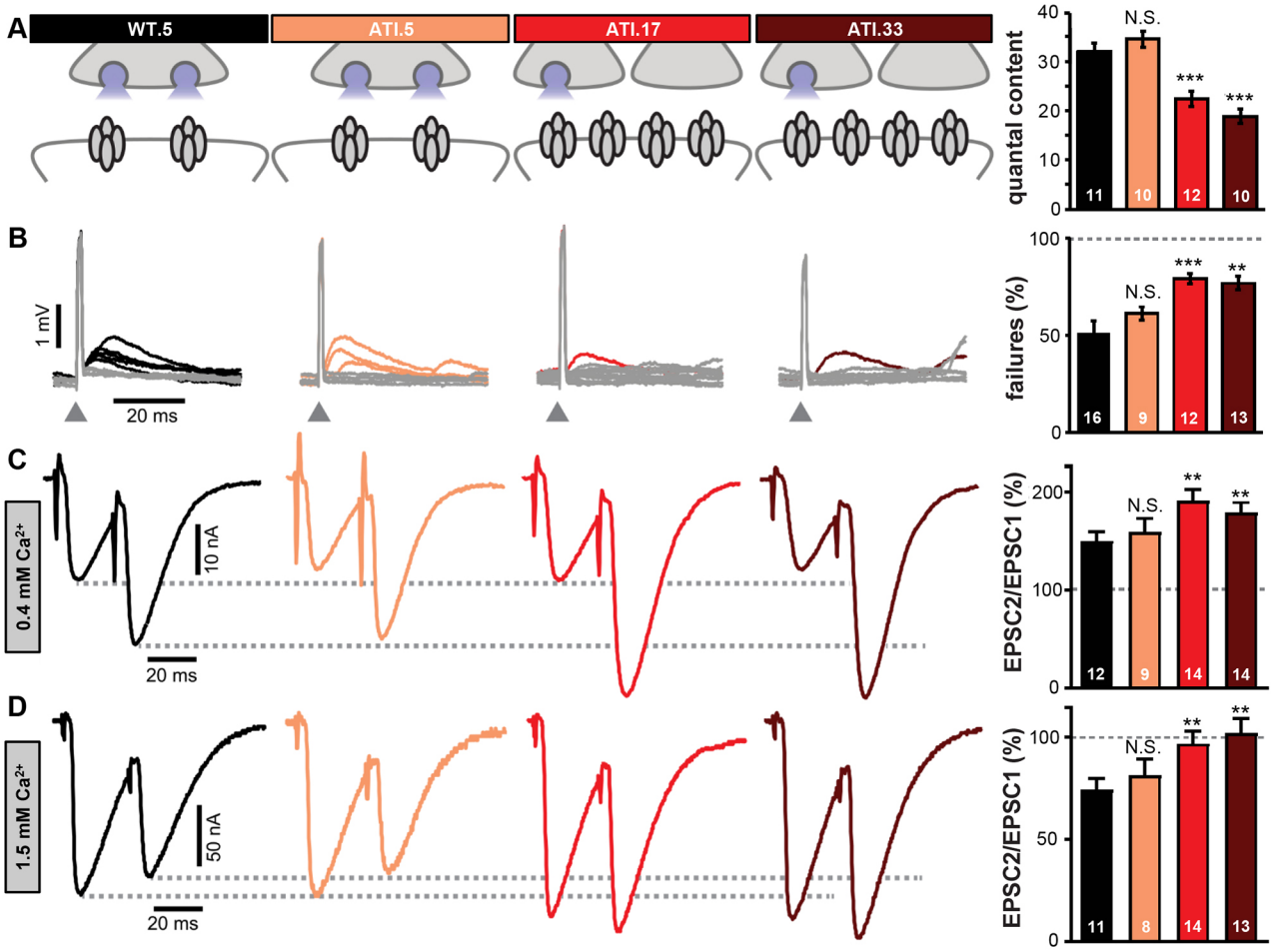

Fig. 5. A potent reduction in neurotransmitter release probability is expressed across the ATI lifespan. (A) Schematic illustrating reduced synaptic strength at later ATI time points. (Right) Quantal content calculated from EPSP and mEPSP data in Figs 1 and 3. (B) Representative traces following stimulation used to perform failure analysis. Gray traces indicate failures and colored traces indicate evoked responses. Eight traces are shown for each genotype. (Right) Quantification of failure rates for each genotype. (C) Representative two electrode voltage clamp (TEVC) traces in lowered extracellular Ca^{2+} showing paired pulse facilitation for each genotype (left) and quantification of the paired pulse ratio (right). (D) Representative TEVC traces showing paired pulse depression in elevated extracellular Ca^{2+} for each genotype (left) and the paired pulse ratio (right). The sample size for each dataset is indicated in each bar. Error bars indicate ±s.e.m. Two-tailed Student's t-test was performed. **P≤0.01; ***P≤0.001; N.S., not significant (P>0.05). Detailed statistical information is shown in Table S5.

Development (2020) 147, dev186312. doi:10.1242/dev.186312

applied the postsynaptic GluR antagonist philanthotoxin-343 (PhTx) (Frank et al., 2006). Incubation for 10 min in PhTx reduces mEPSP amplitude in both wild-type and ATI NMJs, as expected (Fig. S1). In turn, EPSP amplitude is maintained at baseline levels due to a retrograde, homeostatic increase in presynaptic neurotransmitter release in wild type (Goel et al., 2017). Similarly, PHP is robustly expressed across ATI NMJs (Fig. S1). Thus, like PHD and other forms of homeostatic plasticity studied at the *Drosophila* NMJ, the presynaptic inhibition observed at ATI NMJs can be balanced with acute GluR challenge to express PHP and maintain stable synaptic strength.

Extending the larval stage reveals the progression of axonal degeneration in *stathmin* mutants

In our final set of experiments, we considered whether ATI larvae could be used as models for aging and/or neurodegeneration. We hypothesized that NMJs in ATI larvae were unlikely to exhibit classical hallmarks of aging synapses. Although muscle integrity appears to degrade in ATI.33 compared with earlier time points (Fig. 1), synaptic growth (Fig. 2), GluR receptor fields (Fig. 3) and presynaptic function (Fig. 5), all appear similar in ATI.33 relative to earlier time points. Indeed, although reductions in synaptic components and neurotransmission have been observed at aging mammalian NMJs (Li et al., 2018a; Taetzsch and Valdez, 2018), NMJ structure and function remain surprisingly robust in ATI larvae nearing death, with no apparent defects in synaptic function or even PHP plasticity. One additional canonical indicator of aging reported at mammalian NMJs includes presynaptic retractions and fragmentation (Li et al., 2018a; Taetzsch and Valdez, 2018). We therefore assessed synaptic retractions across the ATI lifespan using an established 'footprint' assay, in which a postsynaptic marker is observed to persist without a corresponding presynaptic marker (Eaton et al., 2002; Graf et al., 2011; Perry et al., 2017). However, ATI NMJs, including ATI.33, showed surprisingly stable synapses, with no apparent increases in footprints compared with earlier time points (Fig. 6A,B). Together, these results indicate that NMJ structure, function and integrity remain surprisingly robust across all stages of ATI larvae, even at terminal periods, and are therefore unlikely to serve as a compelling model for age-related synaptic decline.

Although NMJs remain structurally intact and stable across the lifespan of the ATI larvae, this manipulation does enable a substantially longer timescale compared with the typical 5 days of larval development to investigate insults that contribute to neuronal degeneration. We chose to characterize NMJ growth and stability in *stathmin* mutants extended through the ATI manipulation. Stathmin is a tubulin-associated factor involved in maintaining the integrity of the axonal cytoskeleton (Duncan et al., 2013; Lachkar et al., 2010). The mammalian homolog of *Drosophila stathmin* (*SCG10*; also known as *STMN2*) is highly conserved and is thought to function as a surveillance factor for axon damage and degenerative signaling (Shin et al., 2012). In *Drosophila*, loss of *stathmin* leads to a marked increase in NMJ footprints, with more posterior segments showing increased severity relative to more anterior segments (Graf et al., 2011). Surprisingly, *stathmin* mutants are still able to pupate and develop into adults. However, *stathmin* mutants extended in larval stages by the ATI manipulation die shortly after 21 days AEL. We therefore sought to use the ATI system to determine the impact of a prolonged phase of axonal instability in *stathmin* mutants. Indeed, NMJs exhibit increased footprints in *stathmin* mutants extended to ATI.13 time points (stai.13) when compared with stai.5 controls in both frequency (Fig. 6C,D) and severity (Fig. 6E), with the most severe retractions observed in posterior abdominal segments (A3-A5). Finally, we tested whether NMJ growth increased in ATI-extended *stathmin* NMJs, as it does in wild type. Although control ATI synapses grow in bouton and BRP puncta number between 5 and 13 days AEL, *stathmin* NMJs fail to consistently expand (Fig. 6F-H). These experiments highlight the potential of the ATI system to be a useful tool for defining the progression of neurodegeneration at the *Drosophila* NMJ, which is otherwise limited to short larval stages.

DISCUSSION

By arresting further maturation at third instar *Drosophila* larvae, we have been able to accomplish a detailed study of NMJ structure, function and plasticity over much longer timescales than previously possible. This ATI larval system has revealed how the NMJ maintains stable transmission over a vastly extended developmental timescale, in which persistent overgrowth in both pre- and postsynaptic compartments is offset through a potent and homeostatic reduction in neurotransmitter release. Hence, this study not only provides evidence for a potentially novel homeostatic signaling system that balances release probability with synaptic overgrowth, but now extends the temporal window to enable the characterization of a variety of processes, including neurodegeneration, at a powerful model synapse.

As described by Miller et al. (2012), NMJs in third instar larvae that have been developmentally arrested for at least a week beyond the normal time of pupariation continue to grow and add new boutons. Here, we extend this observation to larvae arrested at the third instar for over 30 days, further demonstrating that mechanisms do not exist to suppress or negatively regulate growth when developmental timing is artificially extended. During normal larval growth from first to third instar, the body wall muscles undergo rapid and immense expansion, growing nearly 100-fold in surface area within a few days (Menon et al., 2013). Presynaptic terminals grow and add new boutons in parallel with muscle growth, presumably to maintain stable NMJ strength. In effect, sufficient levels of muscle excitation is sustained through a coordinated increase in all three parameters controlling synaptic physiology: N (number of release sites), P_r (release probability at each site), and Q (quantal size) (Dittman and Ryan, 2019). Hence, during typical stages of larval development, increasing muscle growth requires a concomitant elaboration in NMJs, implying robust signaling systems exist to ensure synaptic size, structure, and function expand in a coordinated manner. This tight structural coupling between muscle fiber and NMJ growth is also observed in mammals and is thought to be a primary mechanism for maintaining NMJ strength during post-developmental muscle growth or wasting (Sanes and Lichtman, 1999, 2001). However, when the normal developmental program is made to continue without terminating in pupariation, NMJ growth continues apparently unchecked, posing a potential challenge of hyperexcitation. There is emerging evidence that when NMJ growth is genetically perturbed, a redistribution of AZ material or adaptations in synapse morphogenesis or postsynaptic neurotransmitter receptors can maintain stable synaptic strength (Goel et al., 2019a,b; Graf et al., 2009). In the case of NMJ overgrowth in *endophilin A* mutants, a homeostatic scaling in AZ size compensates for increased number to lower release probability and maintain stable synaptic strength (Goel et al., 2019a). However, NMJs in ATI larvae do not appear to use such strategies. Rather, a latent form of adaptive plasticity is revealed at ATI NMJs that is sufficiently potent and precise to inhibit

Development (2020) 147, dev186312. doi:10.1242/dev.186312

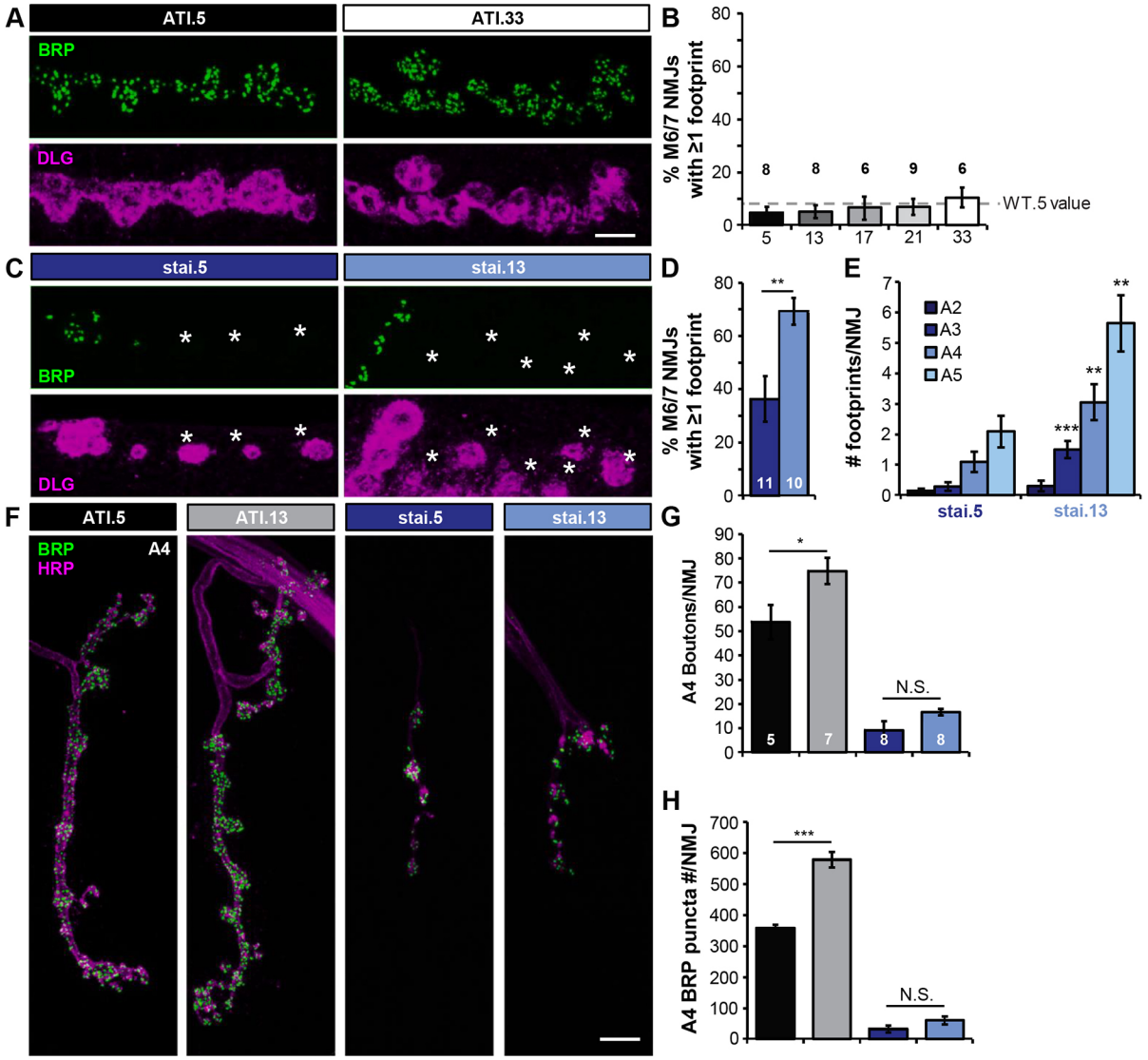

Fig. 6. Extending the larval stage reveals the progression of synaptic retractions in *stathmin* mutants. (A) Representative images of ATI.5 and ATI.33 synapses stained with presynaptic (BRP; green) and postsynaptic (DLG; magenta) markers demonstrating a lack of synaptic retractions at these stages. Scale bar: 5 µm. (B) Quantification of percentage of NMJs at M6/7 with one or more footprints observed across the ATI lifespan (5, 13, 17, 21, 33 AEL). The value for wild type at day 5 is shown by a dashed line (WT.5, *n*=9). (C) Representative BRP and DLG images of *stathmin* mutant NMJs in an ATI background (stai.5 and stai.13; see Table S6 for full genotypes) showing footprints. Asterisks show DLG staining without corresponding BRP. Scale bar: 5 µm in A (for A,C). (D) Quantification of NMJs with one or more footprints in stai.5 and stai.13 animals. (E) Quantification of footprints per NMJ separated by segment in *stathmin* mutants demonstrating more severe retractions on posterior segments (stai.5: A2, *n*=21; A3, *n*=21; A4, *n*=22; A5, *n*=21; stai.13: A2, *n*=20; A3, *n*=20; A4, *n*=19; A5, *n*=20). (F) Representative images of ATI and *stathmin* ATI NMJs at M4 (days 5 and 13) stained with HRP and BRP showing a failure of NMJs to grow in *stai* mutants. Scale bar: 10 µm. (G,H) Quantification of bouton number (G) and BRP puncta number (H; ATI.5, *n*=15; ATI.13, *n*=7; stai.5, *n*=8; stai.13, *n*=8) per NMJ on segment A4 for the indicated genotypes. Colored bars in G and H correspond to genotypes defined in F. The sample size for each dataset is shown above (B) or in (D,G) each bar. Error bars indicate ±s.e.m. Two-tailed Student's *t*-test was performed. **P*≤0.05; ***P*≤0.01; ****P*≤0.001; N.S., not significant (*P*>0.05). Detailed statistical information is shown in Table S6.

neurotransmitter release probability and compensate for the overgrowth of both pre- and postsynaptic compartments.

The presynaptic inhibition of neurotransmitter release that maintains synaptic strength at ATI NMJs is a potentially novel phenomenon of homeostatic plasticity. This form of presynaptic depression appears to be an entirely functional change that reduces release probability, without any apparent adaptations to AZ number, intensity or synaptic structure. Electrophysiologically, the presynaptic inhibition demonstrated at ATI NMJs resembles PHD, a form of homeostatic plasticity characterized at the *Drosophila* NMJ in which excess glutamate release induces a compensatory reduction in release probability that maintains stable synaptic strength (Daniels et al., 2004; Gaviño et al., 2015; Li et al., 2018c). As in PHD, the presynaptic inhibition at ATI NMJs is not reflected in changes to the AZs or synaptic structure (Goel et al., 2019a; Gratz et al., 2019; Li et al., 2018c). However, the only mechanisms known to be capable of inducing PHD require enhanced synaptic vesicle size that results from endocytosis mutants or overexpression of the vesicular glutamate transporter (Daniels et al., 2004; Dickman et al., 2005; Goel et al., 2019a; Verstreken et al., 2002). We found no evidence for changes in synaptic vesicle size at ATI NMJs, as the enhanced postsynaptic glutamate receptor levels observed are sufficient to explain the increased quantal size (Fig. 3) and direct measurement of vesicle size by EM revealed no significant change

Development (2020) 147, dev186312. doi:10.1242/dev.186312

from wild type (Fig. 4). Hence, if the homeostatic depression observed at ATI NMJs is ultimately the same plasticity mechanism as PHD, then this would be the first condition that does not require enlarged synaptic vesicle size. In this case, perhaps excess global glutamate release from increased release sites at ATI NMJs induces the same homeostatic plasticity that increased glutamate released from individual synaptic vesicles does. This would be consistent with a 'glutamate homeostat', responding to excess presynaptic glutamate release, necessary to induce and express PHD (Li et al., 2018c). Alternatively, the presynaptic inhibition triggered at ATI NMJs could be a novel form of PHD, which is induced in response to synaptic overgrowth. Interestingly, although increased postsynaptic glutamate receptor abundance leads to enhanced mEPSP amplitude, no adaptive change in presynaptic function results, which leads to a concomitant increase in synaptic strength (DiAntonio et al., 1999; Li et al., 2018c). One possibility is that a coordinated increase in both pre- and postsynaptic compartments may be necessary to induce the presynaptic inhibition observed at ATI NMJs. The ATI model provides a unique opportunity to interrogate the interplay between developmental growth, adaptive presynaptic inhibition and other homeostatic signaling systems.

Extending the larval stage through the ATI manipulation will circumvent limitations of the brief time window provided by the standard developmental program. Although the ATI model does not appear to exhibit the features described at aging mammalian NMJs (Li et al., 2018a; Taetzsch and Valdez, 2018), we have demonstrated its potential for modeling neurodegenerative conditions by showing the extent of synaptic destabilization caused by loss of *stathmin* that was not fully apparent when restricted to the normal short developmental period in *Drosophila* larvae (Graf et al., 2011). By examining *stathmin* mutant phenotypes in ATI-extended larvae, we were able to observe progressive, time-dependent retractions of presynaptic terminals and gain further insight into the role of *stathmin* in normal NMJ growth and stability. Consistent with the role of *stathmin* in flies, the mammalian homolog *SCG10* is thought to be part of an axonal injury surveillance system, where it accumulates after injury and is involved in regenerative signaling (Shin et al., 2012). More generally, previous studies of degenerative disease models in the larval system have been limited by the brief timespan. For example, one important ALS disease model in flies involves overexpression of repetitive RNAs and peptides derived from the human *C9orf72* gene (Mizielinska et al., 2014; Xu et al., 2013). However, although a variety of progressive and degenerative phenotypes are observed in photoreceptors of adult flies, only the most toxic transgenes are capable of inducing substantial neurodegeneration at the larval NMJ (Perry et al., 2017), likely owing to the limited time frame of typical larval development. The longer timescale enabled by the ATI model therefore provides new opportunities to study progressive phenotypes during neuronal injury, stress and neurodegeneration in addition to the plasticity discussed above in a rapid and genetically tractable system. Indeed, fly models of neurodegenerative conditions such as ALS, Huntington's, Parkinson's and Alzheimer's diseases (McGurk et al., 2015) can benefit from the high-resolution imaging and electrophysiological approaches established at the larval NMJ. The powerful combination of established genetic tools, including binary expression systems (Gal4/UAS, LexA, QF systems; Venken et al., 2011) and emerging CRISPR/Cas9 manipulations (Bier et al., 2018) with the ATI model provides an exciting foundation to gain new insights into synaptic growth, structure, function, plasticity, injury and neurodegeneration over long time frames using the glutamatergic NMJ as a model.

MATERIALS AND METHODS

Fly stocks

Drosophila stocks were raised at 25°C on standard molasses food. The w^{1118} strain is used as the wild-type control unless otherwise noted, as this is the genetic background of the genetic mutants used in this study. ATI larvae were generated by crossing *phm-GAL4* (Gibbens et al., 2011) to *UAS-smox-RNAi* [Bloomington *Drosophila* Stock Center (BDSC), 41670]. *stathmin* mutations were introduced into the ATI background (*stai* allele: BDSC, 16165). All experiments were performed on third instar larvae or ATI larvae of both sexes and at various time points. See Table S8 for a complete list of all stocks and reagents used in this study.

Immunocytochemistry

Third instar male or female larvae were dissected in ice cold Ca^{2+}-free HL-3 and fixed in Bouin's fixative for 5 min as previously described (Kikuma et al., 2017). Briefly, larvae were washed with PBS containing 0.1% Triton X-100 (PBST) for 30 min, blocked for 1 h with 5% normal donkey serum in PBST, and incubated overnight in primary antibodies at 4°C followed by washes and incubation in secondary antibodies. Samples were mounted in VectaShield (Vector Laboratories). The following antibodies were used: mouse anti-Bruchpilot [nc82; 1:100; Developmental Studies Hybridoma Bank (DSHB)]; rabbit anti-DLG (1:10,000; Pielage et al., 2006); guinea pig anti-vGlut (1:2000; Chen et al., 2017); mouse anti-GluRIIA (8B4D2; 1:100; DSHB); affinity purified rabbit anti-GluRIIB (1:1000; Goel and Dickman, 2018); guinea pig anti-GluRIID (1:1000; Kikuma et al., 2019). Donkey anti-mouse, anti-guinea pig and anti-rabbit Alexa Fluor 488-, Cyanine 3 (Cy3)- and DyLight 405-conjugated secondary antibodies (Jackson ImmunoResearch) were used at 1:400. Alexa Fluor 647-conjugated goat anti-HRP (Jackson ImmunoResearch) was used at 1:200. Tetramethylrhodamine (TRITC)-conjugated phalloidin (Thermo Fisher Scientific) was used at 1:1000. All antibody information is summarized in Table S8.

Confocal imaging and analysis

Samples were imaged using a Nikon A1R resonant scanning confocal microscope equipped with NIS Elements software and a 100× APO 1.4NA oil immersion objective using separate channels with four laser lines (405, 488, 561 and 637 nm). For fluorescence quantifications of BRP intensity levels, *z*-stacks were obtained using identical settings for all genotypes with *z*-axis spacing 0.5 µm within an experiment and optimized for detection without saturation of the signal as previously described (Perry et al., 2017). Boutons were counted using vGlut- and HRP-stained Ib NMJ terminals on muscle (M) 4 of segment A2-A4, considering each vGlut punctum to be a bouton. The general analysis toolkit in the NIS Elements software was used for image analysis as previously described (Kikuma et al., 2017). Neuronal surface area was calculated by creating a mask around the HRP channel that labels the neuronal membrane. BRP puncta number, area and total BRP intensity per NMJ were quantified using a bright-spot detection method and filters to binary layers on the BRP-labeled 488 channel in a manner similar to that previously described (Goel et al., 2019b). GluRIIA, GluRIIB and GluRIID puncta intensities were quantified by measuring the total sum intensity of each individual GluR punctum and these values were then averaged per NMJ to get one sample measurement (*n*). For NMJ retraction analysis, footprints were scored by eye as reported in Eaton et al. (2002) on M6/7 segments A2-A5. Anti-DLG was used as a postsynaptic marker and either anti-vGlut or anti-BRP for a presynaptic marker (wild-type controls yielded similar retraction scores for either presynaptic marker).

Electron microscopy (EM)

EM analysis was performed as previously described (Russo et al., 2019) with minor modifications. Wandering third instar larvae were dissected in Ca^{2+}-free HL-3 and then fixed in 4% paraformaldehyde prepared by mixing 16% paraformaldehyde (aqueous, EMS, 15700) in PBS at 4°C. The larval pelts were stored in this fixative at 4°C. On the day of preparation, larvae were transferred to 1% glutaraldehyde in distilled water for 1 h at room temperature, then washed 3× for 5 min in distilled water. The larval pelts were then placed in 1% osmium tetroxide in distilled water for 90 min at room temperature and in ferracyanide-reduced osmium tetraoxide for

Development (2020) 147, dev186312. doi:10.1242/dev.186312

90 min. After washing 3× in water, larvae were dehydrated in a graded acetone series, infiltrated with 50% uncatalyzed Spurr's resin in acetone for 24 h, followed by two 24 h changes of 100% uncatalyzed Spurr's and polymerization in freshly catalyzed Spurr's for 24 h at 60°C. Then 60 nm sections were collected on Formvar-coated 2×1 mm slot grids, stained with 2% uranyl acetate and Reynolds lead citrate and imaged by transmission EM at 80 kV in a Zeiss EM10 equipped with an Erlangshen CCD camera (Gatan). Images were analyzed blind to genotype using measurement tools in the ImageJ software. The outer diameter of each synaptic vesicle within a 300 nm radius from the center of an active zone within a bouton was quantified for all genotypes.

Electrophysiology

All dissections and recordings were performed in modified HL-3 saline (Stewart et al., 1994; Dickman et al., 2005; Kiragasi et al., 2017) containing 70 mM NaCl, 5 mM KCl, 10 mM $MgCl_2$, 10 mM $NaHCO_3$, 115 mM sucrose, 5 mM Trehalose, 5 mM HEPES and 0.4 mM $CaCl_2$ (pH 7.2). NMJ sharp electrode (electrode resistance of 10-30 MΩ) recordings were performed on M6 and M7 of abdominal segments A2 and A3 in wandering third instar larvae as previously described (Goel et al., 2019a). Recordings were performed on an Olympus BX61 WI microscope using a 40×/0.80 water-dipping objective, and acquired using an Axoclamp 900A amplifier, Digidata 1440A acquisition system and pClamp 10.5 software (Molecular Devices). Electrophysiological sweeps were digitized at 10 kHz and filtered at 1 kHz. Data were analyzed using Clampfit (Molecular Devices), MiniAnalysis (Synaptosoft) and Excel (Microsoft) software.

mEPSPs were recorded in the absence of any stimulation and cut motor axons were stimulated to elicit EPSPs. Average mEPSP, EPSP and quantal content were calculated for each genotype by dividing EPSP amplitude by mEPSP amplitude. Muscle input resistance (R_{in}) and resting membrane potential (V_{rest}) were monitored during each experiment. Recordings were rejected if the V_{rest} was above −60 mV, if the R_{in} was less than 5 MΩ, or if either measurement deviated by more than 10% during the course of the experiment. Larvae were incubated with or without philanthotoxin-433 (PhTx; Sigma-Aldrich; 20 µM) and resuspended in HL-3 for 10 min, as previously described (Frank et al., 2006; Dickman and Davis, 2009).

Failure analysis was performed in HL-3 solution containing 0.15 mM $CaCl_2$, which resulted in failures in about half of the stimulated responses in wild-type larvae. A total of 40 trials (stimulations) were performed at each NMJ in all genotypes. Failure rate was obtained by dividing the total number of failures by the total number of trials (40). Paired-pulse recordings were performed at a Ca^{2+} concentration of 0.3 mM to assay PPF and 1.5 mM for PPD. Following the first stimulation, a second excitatory postsynaptic current (EPSC) was evoked at an interstimulus interval of 16.67 ms (60 Hz). Paired-pulse ratios were calculated as the EPSC amplitude of the second response divided by the first response (EPSC2/EPSC1).

Experimental design and statistical analysis

For electrophysiological and immunostaining experiments, each NMJ terminal (M6 for physiology, M4 for immunostaining analyses) is considered an *n* of 1, as each presynaptic motor neuron terminal is confined to its own muscle hemi-segment. For these experiments, M4 or M6 were analyzed from hemi-segments A2-A4 from each larva, typically two NMJs per animal per experiment. To control for variability between larvae within a genotype, NMJs were analyzed from at least five individual larvae. See Tables S1-S7 for additional details.

Statistical analysis was performed using GraphPad Prism (version 7.0) or Microsoft Excel software (version 16.22). Data were assessed for normality using a D'Agostino-Pearson omnibus normality test, which determined that the assumption of normality of the sample distribution was not violated. Normally distributed data were analyzed for statistical significance using a Student's *t*-test (pairwise comparison) or an analysis of variance (ANOVA) and Tukey's test for multiple comparisons. Data were then compared using either a one-way ANOVA and tested for significance using a Tukey's multiple comparison test or using an unpaired 2-tailed Student's *t*-test with Welch's correction. All data are presented as mean±s.e.m. with varying levels of significance assessed as $*P \leq 0.05$, $**P \leq 0.01$, $***P \leq 0.001$ (N.S., not significant). See Tables S1-S7 for additional statistical details and values.

Acknowledgements

We thank Naoki Yamanaka (University of California, Riverside, CA, USA) and Mike O'Connor (University of Minnesota, MN, USA) who sent us other RNAi lines to test for the ATI model. We also thank the Bloomington *Drosophila* Stock Center and Developmental Studies Hybridoma Bank for additional stocks and reagents (National Institutes of Health grant P40OD018537).

Competing interests

The authors declare no competing or financial interests.

Author contributions

Conceptualization: D.D., B.G., D.L.M., S.P., P.G.; Methodology: D.D., B.G., D.L.M., C.B., S.P., P.G.; Formal analysis: D.D., N.L.T., S.P., P.G.; Investigation: D.L.M., C.P., S.P., P.G.; Resources: D.D., B.G., D.L.M., C.B.; Data curation: N.L.T., S.P., P.G.; Writing - original draft: D.D., S.P.; Writing - review & editing: D.D., B.G., D.L.M., S.P., P.G.; Supervision: D.D.; Project administration: D.D.; Funding acquisition: D.D., C.B.

Funding

This study was supported by a fellowship from the National Institute of General Medical Sciences to S.P. (F32GM130108) and grants from the National Institute of Neurological Disorders and Stroke to D.D. (NS111414 and NS091546). Deposited in PMC for release after 12 months.

Supplementary information

Supplementary information available online at
http://dev.biologists.org/lookup/doi/10.1242/dev.186312.supplemental

Peer review history

The peer review history is available online at
https://dev.biologists.org/lookup/doi/10.1242/dev.186312.reviewer-comments.pdf

References

Akbergenova, Y., Cunningham, K. L., Zhang, Y. V., Weiss, S. and Littleton, J. T. (2018). Characterization of developmental and molecular factors underlying release heterogeneity at *Drosophila* synapses. *Elife* **7**, e38268. doi:10.7554/eLife.38268.030

Atwood, H. L., Govind, C. K. and Wu, C.-F. (1993). Differential ultrastructure of synaptic terminals on ventral longitudinal abdominal muscles in *Drosophila* larvae. *J. Neurobiol.* **24**, 1008-1024. doi:10.1002/neu.480240803

Bier, E., Harrison, M. M., O'Connor-Giles, K. M. and Wildonger, J. (2018). Advances in engineering the fly genome with the CRISPR-Cas system. *Genetics* **208**, 1-18. doi:10.1534/genetics.117.1113

Böhme, M. A., Beis, C., Reddy-Alla, S., Reynolds, E., Mampell, M. M., Grasskamp, A. T., Lützkendorf, J., Bergeron, D. D., Driller, J. H., Babikir, H. et al. (2016). Active zone scaffolds differentially accumulate Unc13 isoforms to tune Ca^{2+} channel-vesicle coupling. *Nat. Neurosci.* **19**, 1311-1320. doi:10.1038/nn.4364

Brummel, T., Abdollah, S., Haerry, T. E., Shimell, M. J., Merriam, J., Raftery, L., Wrana, J. L. and O'Connor, M. B. (1999). The Drosophila Activin receptor Baboon signals through dSmad2 and controls cell proliferation but not patterning during larval development. *Genes Dev.* **13**, 98-111. doi:10.1101/gad.13.1.98

Chen, X., Ma, W., Zhang, S., Paluch, J., Guo, W. and Dickman, D. (2017). The BLOC-1 subunit pallidin facilitates activity-dependent synaptic vesicle recycling. *eNeuro* **4**, ENEURO.0335-16.2017. doi:10.1523/ENEURO.0335-16.2017

Daniels, R. W., Collins, C. A., Gelfand, M. V., Dant, J., Brooks, E. S., Krantz, D. E. and DiAntonio, A. (2004). Increased expression of the *Drosophila* vesicular glutamate transporter leads to excess glutamate release and a compensatory decrease in quantal content. *J. Neurosci.* **24**, 10466-10474. doi:10.1523/JNEUROSCI.3001-04.2004

Danielsen, E. T., Moeller, M. E., Yamanaka, N., Ou, Q., Laursen, J. M., Soenderholm, C., Zhuo, R., Phelps, B., Tang, K., Zeng, J. et al. (2016). A *Drosophila* genome-wide screen indentifies regulators of steroid hormone production and developmental timing. *Dev. Cell.* **37**, 558-570. doi:10.1016/j.devcel.2016.05.015

Davis, G. W. and Goodman, C. S. (1998). Genetic analysis of synaptic development and plasticity: homeostatic regulation of synaptic efficacy. *Curr. Opin. Neurobiol.* **8**, 149-156. doi:10.1016/S0959-4388(98)80018-4

DiAntonio, A., Petersen, S. A., Heckmann, M. and Goodman, C. S. (1999). Glutamate receptor expression regulates quantal size and quantal content at the *Drosophila* neuromuscular junction. *J. Neurosci.* **19**, 3023-3032. doi:10.1523/JNEUROSCI.19-08-03023.1999

Dickman, D. K. and Davis, G. W. (2009). The schizophrenia susceptibility gene dysbindin controls synaptic homeostasis. *Science* **326**, 1127-1130. doi:10.1126/science.1179685

Dickman, D. K., Horne, J. A., Meinertzhagen, I. A. and Schwarz, T. L. (2005). A slowed classical pathway rather than kiss-and-run mediates endocytosis at

synapses lacking synaptojanin and endophilin. *Cell* **123**, 521-533. doi:10.1016/j.cell.2005.09.026
Dittman, J. S. and Ryan, T. A. (2019). The control of release probability at nerve terminals. *Nat. Rev. Neurosci.* **20**, 177-186. doi:10.1038/s41583-018-0111-3
Duncan, J. E., Lytle, N. K., Zuniga, A. and Goldstein, L. S. B. (2013). The microtubule regulatory protein stathmin is required to maintain the integrity of axonal microtubules in *Drosophila*. *PLoS ONE* **8**, e68324. doi:10.1371/journal.pone.0068324
Eaton, B. A., Fetter, R. D. and Davis, G. W. (2002). Dynactin is necessary for synapse stabilization. *Neuron* **34**, 729-741. doi:10.1016/S0896-6273(02)00721-3
Frank, C. A., Kennedy, M. J., Goold, C. P., Marek, K. W. and Davis, G. W. (2006). Mechanisms underlying the rapid induction and sustained expression of synaptic homeostasis. *Neuron* **52**, 663-677. doi:10.1016/j.neuron.2006.09.029
Frank, C. A., James, T. D. and Müller, M. (2020). Homeostatic control of *Drosophila* neuromuscular junction function. *Synapse* **74**, e22133. doi:10.1002/syn.22133
Gaviño, M. A., Ford, K. J., Archila, S. and Davis, G. W. (2015). Homeostatic synaptic depression is achieved through a regulated decrease in presynaptic calcium channel abundance. *Elife* **4**, e05473. doi:10.7554/eLife.05473.011
Gibbens, Y. Y., Warren, J. T., Gilbert, L. I. and O'Connor, M. B. (2011). Neuroendocrine regulation of *Drosophila* metamorphosis requires TGFbeta/Activin signaling. *Development* **138**, 2693-2703. doi:10.1242/dev.063412
Goel, P. and Dickman, D. (2018). Distinct homeostatic modulations stabilize reduced postsynaptic receptivity in response to presynpatic DLK signaling. *Nat. Commun.* **9**, 1856. doi:10.1038/s41467-018-04270-0
Goel, P., Li, X. and Dickman, D. (2017). Disparate postsynaptic induction mechanisms ultimately converge to drive the retrograde enhancement of presynaptic efficacy. *Cell Rep.* **21**, 2339-2347. doi:10.1016/j.celrep.2017.10.116
Goel, P., Dufour Bergeron, D., Böhme, M. A., Nunnelly, L., Lehmann, M., Buser, C., Walter, A. M., Sigrist, S. J. and Dickman, D. (2019a). Homeostatic scaling of active zone scaffolds maintains global synaptic strength. *J. Cell Biol.* **218**, 1706-1724. doi:10.1083/jcb.201807165
Goel, P., Khan, M., Howard, S., Kim, G., Kiragasi, B., Kikuma, K. and Dickman, D. (2019b). A screen for synaptic growth mutants reveals mechanisms that stabilize synaptic strength. *J. Neurosci.* **39**, 4051-4065. doi:10.1523/JNEUROSCI.2601-18.2019
Graf, E. R., Daniels, R. W., Burgess, R. W., Schwarz, T. L. and DiAntonio, A. (2009). Rab3 dynamically controls protein composition at active zones. *Neuron* **64**, 663-677. doi:10.1016/j.neuron.2009.11.002
Graf, E. R., Heerssen, H. M., Wright, C. M., Davis, G. W. and DiAntonio, A. (2011). Stathmin is required for stability of the Drosophila neuromuscular junction. *J. Neurosci.* **31**, 15026-15034. doi:10.1523/JNEUROSCI.2024-11.2011
Gratz, S. J., Goel, P., Bruckner, J. J., Hernandez, R. X., Khateeb, K., Macleod, G. T., Dickman, D. and O'Connor-Giles, K. M. (2019). Endogenous tagging reveals differential regulation of Ca2+ channels at single active zones during presynaptic homeostatic potentiation and depression. *J. Neurosci.* **39**, 2416-2429. doi:10.1523/JNEUROSCI.3068-18.2019
Han, T. H., Dharkar, P., Mayer, M. L. and Serpe, M. (2015). Functional reconstitution of *Drosophila melanogaster* NMJ glutamate receptors. *Proc. Natl. Acad. Sci. USA* **112**, 6182-6187. doi:10.1073/pnas.1500458112
Hevia, C. F., López-Varea, A., Esteban, N. and de Celis, J. F. (2017). A search for genes mediating the growth-promoting function of TGFβ in the *Drosophila melanogaster* wing disc. *Genetics* **206**, 231-249. doi:10.1534/genetics.116.197228
Kikuma, K., Li, X., Kim, D., Sutter, D. and Dickman, D. K. (2017). Extended synaptotagmin localizes to presynaptic ER and promotes neurotransmission and synaptic growth in *Drosophila*. *Genetics.* **207**, 993-1006. doi:10.1534/genetics.117.300261
Kikuma, K., Li, X., Perry, S., Li, Q., Goel, P., Chen, C., Kim, D., Stravropoulos, N. and Dickman, D. (2019). Cul3 and insomniac are required for rapid ubiquitination of postsynaptic targets and retrograde homeostatic signaling. *Nat. Commun.* **10**, 2998. doi:10.1038/s41467-019-10992-6
Kiragasi, B., Wondolowski, J., Li, Y. and Dickman, D. K. (2017). A presynaptic glutamate receptor subunit confers robustness to neurotransmission and homeostatic potentiation. *Cell Reports* **19**, 2694-2706. doi:10.1016/j.celrep.2017.06.003
Kittel, R. J., Wichmann, C., Rasse, T. M., Fouquet, W., Schmidt, M., Schmid, A., Wagh, D. A., Pawlu, C., Kellner, R. R., Willig, K. I. et al. (2006). Bruchpilot promotes active zone assembly, Ca2+ channel clustering, and vesicle release. *Science* **312**, 1051-1054. doi:10.1126/science.1126308
Lachkar, S., Lebois, M., Steinmetz, M. O., Guichet, A., Lal, N., Curmi, P. A., Sobel, A. and Ozon, S. (2010). *Drosophila* stathmins bind tubulin heterodimers with high and variable stoichiometries. *J. Biol. Chem.* **285**, 11667-11680. doi:10.1074/jbc.M109.096727
Li, L., Xiong, W.-C. and Mei, L. (2018a). Neuromuscular junction formation, aging, and disorders. *Annu. Rev. Physiol.* **80**, 159-188. doi:10.1146/annurev-physiol-022516-034255
Li, X., Goel, P., Chen, C., Angajala, V., Chen, X. and Dickman, D. K. (2018b). Synapse-specific and compartmentalized expression of presynaptic homeostatic potentiation. *Elife* **7**, e34338. doi:10.7554/eLife.34338
Li, X., Goel, P., Wondolowski, J., Paluch, J. and Dickman, D. (2018c). A glutamate homeostat controls the presynaptic inhibition of neurotransmitter release. *Cell Rep.* **23**, 1716-1727. doi:10.1016/j.celrep.2018.03.130
Li, J., Park, E., Zhong, L. and Chen, L. (2019). Homeostatic synaptic plasticity as a metaplasticity mechanism - a molecular and cellular perspective. *Curr. Opin. Neurobiol.* **54**, 44-53. doi:10.1016/j.conb.2018.08.010
McGurk, L., Berson, A. and Bonini, N. M. (2015). *Drosophila* as an In Vivo model for human neurodegenerative disease. *Genetics* **201**, 377-402. doi:10.1534/genetics.115.179457
Menon, K. P., Carrillo, R. A. and Zinn, K. (2013). Development and plasticity of the *Drosophila* larval neuromuscular junction. *Wiley Interdiscip. Rev. Dev. Biol.* **2**, 647-670. doi:10.1002/wdev.108
Miller, D. L., Ballard, S. L. and Ganetzky, B. (2012). Analysis of synaptic growth and function in *Drosophila* with an extended larval stage. *J. Neurosci.* **32**, 13776-13786. doi:10.1523/JNEUROSCI.0508-12.2012
Mizielinska, S., Grönke, S., Niccoli, T., Ridler, C. E., Clayton, E. L., Devoy, A., Moens, T., Norona, F. E., Woollacott, I. O. C., Pietrzyk, J. et al. (2014). C9orf72 repeat expansions cause neurodegeneration in *Drosophila* through arginine-rich proteins. *Science* **345**, 1192-1194. doi:10.1126/science.1256800
Nelson, S. B. and Valakh, V. (2015). Excitatory/inhibitory balance and circuit homeostasis in autism spectrum disorders. *Neuron* **87**, 684-698. doi:10.1016/j.neuron.2015.07.033
Ohhara, Y., Kobayashi, S. and Yamanaka, N. (2017). Nutrient-dependent endocycling in steroidogenic tissue dictates timing of metamorphosis in *Drosophila melanogaster*. *PLoS Genet.* **13**, e1006583. doi:10.1371/journal.pgen.1006583
Ono, H., Rewitz, K. F., Shinoda, T., Itoyama, K., Petryk, A., Rybczynski, R., Jarcho, M., Warren, J. T., Marqués, G., Shimell, M. J. et al. (2006). Spook and Spookier code for stage-specific components of the ecdysone biosynthesis pathway in Diptera. *Dev. Biol.* **298**, 555-570. doi:10.1016/j.ydbio.2006.07.023
Perry, S., Han, Y., Das, A. and Dickman, D. (2017). Homeostatic plasticity can be induced and expressed to restore synaptic strength at neuromuscular junctions undergoing ALS-related degeneration. *Hum. Mol. Genet.* **26**, 4153-4167. doi:10.1093/hmg/ddx304
Petersen, S. A., Fetter, R. D., Noordermeer, J. N., Goodman, C. S. and DiAntonio, A. (1997). Genetic analysis of glutamate receptors in *Drosophila* reveals a retrograde signal regulating presynaptic transmitter release. *Neuron* **19**, 1237-1248. doi:10.1016/S0896-6273(00)80415-8
Pielage, J., Fetter, R. D. and Davis, G. W. (2006). A postsynaptic spectrin scaffold defines active zone size, spacing, and efficacy at the *Drosophila* neuromuscular junction. *J. Cell Biol.* **175**, 491-503. doi:10.1083/jcb.200607036
Pozo, K. and Goda, Y. (2010). Unraveling mechanisms of homeostatic synaptic plasticity. *Neuron* **66**, 337-351. doi:10.1016/j.neuron.2010.04.028
Qin, G., Schwarz, T., Kittel, R. J., Schmid, A., Rasse, T. M., Kappei, D., Ponimaskin, E., Heckmann, M. and Sigrist, S. J. (2005). Four different subunits are essential for expressing the synaptic glutamate receptor at neuromuscular junctions of *Drosophila*. *J. Neurosci.* **25**, 3209-3218. doi:10.1523/JNEUROSCI.4194-04.2005
Rewitz, K. F., Yamanaka, N., Gilbert, L. I. and O'Connor, M. B. (2009). The insect neuropeptide PTTH activates receptor tyrosine kinase torso to initiate metamorphosis. *Science* **326**, 1403-1405. doi:10.1126/science.1176450
Russo, A., Goel, P., Brace, E. J., Buser, C., Dickman, D. and DiAntonio, A. (2019). The E3 ligase Highwire promotes synaptic transmission by targeting the NAD-synthesizing enzyme dNmnat. *EMBO Rep.* **20**, e46975. doi:10.15252/embr.201846975
Sanes, J. R. and Lichtman, J. W. (1999). Development of the vertebrate neuromuscular junction. *Annu. Rev. Neurosci.* **22**, 389-442. doi:10.1146/annurev.neuro.22.1.389
Sanes, J. R. and Lichtman, J. W. (2001). Induction, assembly, maturation and maintenance of a postsynaptic apparatus. *Nat. Rev. Neurosci.* **2**, 791-805. doi:10.1038/35097557
Schuster, C. M., Davis, G. W., Fetter, R. D. and Goodman, C. S. (1996). Genetic dissection of structural and functional components of synaptic plasticity. I. Fasciclin II controls synaptic stabilization and growth. *Neuron* **17**, 641-654.
Shin, J. E., Miller, B. R., Babetto, E., Cho, Y., Sasaki, Y., Qayum, S., Russier, E. V., Cavalli, V., Milbrandt, J. and DiAntonio, A. (2012). SCG10 is a JNK target in the axonal degeneration pathway. *Proc. Natl. Acad. Sci. USA* **109**, 3696-3705. doi:10.1073/pnas.1216204109
Stewart, B. A., Atwood, H. L., Renger, J. J., Wang, J. and Wu, C.-F. (1994). Improved stability of *Drosophila* larval neuromuscular preparations in haemolymph-like phsiological solutions. *J. Comp. Physiol. A Neuroethol. Sens. Neural Behav. Physiol.* **175**, 179-191. doi:10.1007/BF00215114
Taetzsch, T. and Valdez, G. (2018). NMJ maintenance and repair in aging. *Curr. Opin. Physiol.* **4**, 57-64. doi:10.1016/j.cophys.2018.05.007
Turrigiano, G. (2012). Homeostatic synaptic plasticity: local and global mechanisms for stabilizing neuronal function. *Cold Spring Harb. Perspect. Biol.* **4**, a005736-a005736. doi:10.1101/cshperspect.a005736
Venken, K. J. T., Simpson, J. H. and Bellen, H. J. (2011). Genetic manipulation of genes and cells in the nervous system of the fruit fly. *Neuron* **72**, 202-230. doi:10.1016/j.neuron.2011.09.021

Verstreken, P., Kjaerulff, O., Lloyd, T. E., Atkinson, R., Zhou, Y., Meinertzhagen, I. A. and Bellen, H. J. (2002). Endophilin mutations block clathrin-mediated endocytosis but not neurotransmitter release. *Cell* **109**, 101-112. doi:10.1016/S0092-8674(02)00688-8

Wagh, D. A., Rasse, T. M., Asan, E., Hofbauer, A., Schwenkert, I., Dürrbeck, H., Buchner, S., Dabauvalle, M.-C., Schmidt, M., Qin, G. et al. (2006). Bruchpilot, a protein with homology to ELKS/CAST, is required for structural integrity and function of synaptic active zones in *Drosophila*. *Neuron* **49**, 833-844. doi:10.1016/j.neuron.2006.02.008

Walkiewicz, M. A. and Stern, M. (2009). Increased insulin/insulin growth factor signaling advances the onset of metamorphosis in *Drosophila*. *PLoS ONE* **4**, e5072. doi:10.1371/journal.pone.0005072

Wondolowski, J. and Dickman, D. (2013). Emerging links between homeostatic synaptic plasticity and neurological disease. *Front. Cell. Neurosci.* **7**, 223. doi:10.3389/fncel.2013.00223

Xu, Z., Poidevin, M., Li, X., Li, Y., Shu, L., Nelson, D. L., Li, H., Hales, C. M., Gearing, M., Wingo, T. S. et al. (2013). Expanded GGGGCC repeat RNA associated with amyotrophic lateral sclerosis and frontotemporal dementia causes neurodegeneration. *Proc. Natl. Acad. Sci. USA* **110**, 7778-7783. doi:10.1073/pnas.1219643110

Yamanaka, N., Rewitz, K. F. and O'Connor, M. B. (2013). Ecdysone control of developmental transitions: lessons from *Drosophila* research. *Annu. Rev. Entomol.* **58**, 497-516. doi:10.1146/annurev-ento-120811-153608

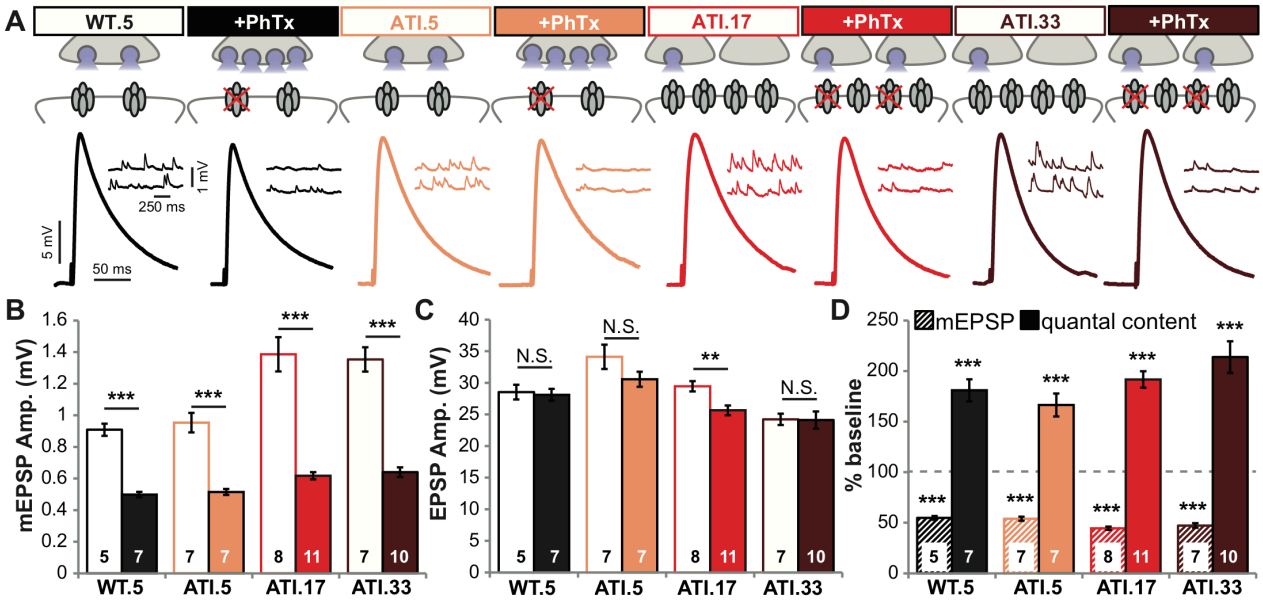

Figure S1: Presynaptic homeostatic potentiation can be induced and expressed across the ATI lifespan. (A) (Top) Schematic illustrating baseline and +PhTx conditions at NMJs for each genotype. (Bottom) Representative EPSP and mEPSP traces for each genotype at baseline and +PhTx. **(B-D)** Quantification of mEPSP amplitude (B), EPSP amplitude (C), and mEPSP and quantal content values following PhTx application normalized as a percentage of baseline values (-PhTx) (D) in the indicated genotypes. The sample size for each data set is indicated in each bar. Error bars indicate ±SEM. Two- tailed Student's T-Test was performed. **p≤0.01; ***p≤0.001; N.S. = not significant, p>0.05. Detailed statistical information is shown in Table S7.

Table S1. Data and statistical information. All absolute values (mean, SEM, N) and statistical information (tests used and P-values) for all data points shown in Fig.1 are shown.

Figure 1:

Symbol	Genotype	Time Point days AEL	Muscle surface area μm^2 (± SEM, N)	Input resistance MΩ (± SEM, N)	EPSP amplitude mV (± SEM, N)
WT.5	*w^{1118}*	5	54187.28 (2327.86, 10)	6.11 (0.31, 13)	30.25 (0.87, 15)
ATI.5	*UAS-smox-RNAi/+; phm-Gal4/+*	5	49086.17 (2581.39, 10)	6 (0.32, 10)	29.71 (0.95, 11)
ATI.9	*UAS-smox-RNAi/+; phm-Gal4/+*	9	63157.11 (3264.28, 10)		
ATI.13	*UAS-smox-RNAi/+; phm-Gal4/+*	13	64947.26 (1929.30, 9)	4.33 (0.42, 6)	29.36 (1.59, 6)
ATI.17	*UAS-smox-RNAi/+; phm-Gal4/+*	17	75962.95 (2756.79, 10)	2.41 (0.35, 19)	31.03 (0.99, 21)
ATI.21	*UAS-smox-RNAi/+; phm-Gal4/+*	21	73533.58 (5041.38, 10)	2.16 (0.19, 9)	27.08 (1.91, 9)
ATI.25	*UAS-smox-RNAi/+; phm-Gal4/+*	25	65459.34 (4755.70, 10)		
ATI.29	*UAS-smox-RNAi/+; phm-Gal4/+*	29	60284.69 (1918.83, 10)		
ATI.33	*UAS-smox-RNAi/+; phm-Gal4/+*	33	62156.54 (3388.91, 10)	3.25 (0.21, 16)	28.89 (0.89, 19)

Statistical Analysis: 1-way ANOVA with Tukey's multiple-comparison test

Array 1	Array 2	P-value	Symbol
WT.5 EPSP	ATI.5 EPSP	0.9993	N.S.
WT.5 EPSP	ATI.17 EPSP	0.9970	N.S.
WT.5 EPSP	ATI.33 EPSP	0.8105	N.S.

Table S2. Data and statistical information. All absolute values (mean, SEM, N) and statistical information (tests used and P-values) for all data points shown in Fig. 2 are shown.

Symbol	Neuronal S.A. (M4-Ib) µm² (± SEM)	Boutons M4-Ib # (± SEM)	BRP puncta # (± SEM)	BRP puncta size µm² (± SEM)	BRP puncta mean intensity % WT.5 (± SEM)	N
WT.5	238.18 (10.03)	47.54 (2.44)	370.11 (12.01)	0.089 (0.0037)	100 (2.47)	28
ATI.5	237.07 (10.65)	54.7 (3.9)	377.8 (13.63)	0.084 (0.0022)	105.07 (1.89)	10
ATI.9	380.93 (24.62)	78.6 (6.97)	628.8 (28.77)	0.085 (0.0022)	93.12 (2.61)	10
ATI.13	367.88 (25.54)	88.2 (5.89)	681.71 (29.02)	0.07 (0.0031)	91.85 (1.72)	10
ATI.17	446.01 (22.63)	106.2 (10.72)	857.5 (37.7)	0.12 (0.0067)	134.44 (6.19)	10
ATI.21	545.13 (38.91)	108.4 (6.06)	991.7 (65.04)	0.103 (0.0102)	117.7 (9.98)	10
ATI.25	566.35 (53.63)	101.2 (4.77)	1042.8 (30.09)	0.108 (0.0047)	115.21 (3.98)	10
ATI.29	529.16 (35.02)	104.6 (10.61)	903.3 (40.15)	0.059 (0.006)	84.37 (3.07)	10
ATI.33	552.775 (20.11)	105.4 (7.75)	843.1 (39.06)	0.038 (0.0074)	73.69 (4.27)	10

Statistical Analysis: 1-way ANOVA with Tukey's multiple-comparison test

Array 1	Array 2	P-value	Symbol
WT.5 neuronal S.A.	ATI.5 neuronal S.A.	0.9981	N.S.
WT.5 neuronal S.A.	ATI.9 neuronal S.A.	0.0002	***
WT.5 neuronal S.A.	ATI.13 neuronal S.A.	7.05221E-05	***
WT.5 neuronal S.A.	ATI.17 neuronal S.A.	1.88305E-06	***
WT.5 neuronal S.A.	ATI.21 neuronal S.A.	1.63492E-05	***
WT.5 neuronal S.A.	ATI.25 neuronal S.A.	0.0002	***
WT.5 neuronal S.A.	ATI.29 neuronal S.A.	1.0958E-05	***
WT.5 neuronal S.A.	ATI.33 neuronal S.A.	6.82933E-09	***
WT.5 bouton #	ATI.5 bouton #	0.2659	N.S.
WT.5 bouton #	ATI.9 bouton #	0.0022	**
WT.5 bouton #	ATI.13 bouton #	5.2751E-05	***
WT.5 bouton #	ATI.17 bouton #	0.0004	***
WT.5 bouton #	ATI.21 bouton #	1.94878E-06	***
WT.5 bouton #	ATI.25 bouton #	2.51313E-07	***
WT.5 bouton #	ATI.29 bouton #	0.0005	***
WT.5 bouton #	ATI.33 bouton #	4.16423E-05	***
WT.5 BRP #	ATI.5 BRP #	0.7498	N.S.
WT.5 BRP #	ATI.9 BRP #	4.28242E-06	***
WT.5 BRP #	ATI.13 BRP #	4.86698E-07	***
WT.5 BRP #	ATI.17 BRP #	2.16702E-07	***
WT.5 BRP #	ATI.21 BRP #	5.97535E-06	***
WT.5 BRP #	ATI.25 BRP #	3.15421E-10	***
WT.5 BRP #	ATI.29 BRP #	1.60783E-07	***
WT.5 BRP #	ATI.33 BRP #	3.92474E-07	***

Table S3. Data and statistical information. All absolute values (mean, SEM, N) and statistical information (tests used and P-values) for all data points shown in Fig. 3 are shown.

Symbol	GluRIID puncta M4-Ib # (± SEM)	Puncta sum intensity (IIA, IIB, IID) % WT.5 (± SEM)	N	mEPSP Amp. mV (± SEM, N)	mEPSP freq. Hz (± SEM, N)	decay Tau ms (± SEM, N)
WT.5	299.43 (11.13)	100 (2.84) 100 (1.97) 100 (4.01)	40	0.9308 (0.0411, 11)	2.857 (0.1437, 14)	29.99 (1.228, 11)
ATI.5	325.95 (23.8)	80.13 (8.72) 83.49 (3.49) 98.75 (14.29)	20	0.8799 (0.0276, 10)	3.056 (0.1818, 9)	30.14 (1.285, 8)
ATI.17	761.05 (30.61)	149.8 (10.97) 143.46 (9.38) 132.59 (10.85)	20	1.3285 (0.0657, 12)	3.851 (0.1824, 12)	32.32 (1.026, 9)
ATI.33	801.64 (25.18)	113.09 (7.1) 130.63 (9.94) 118.81 (10.26)	22	1.47 (0.0664, 10)	3.803 (0.1845, 15)	34.14 (1.454, 9)

Statistical Analysis: 2-tailed Student's T-test

Array 1	Array 2	P-value	Symbol
WT.5 GluRIID #	ATI.5 GluRIID #	0.253233954	N.S.
WT.5 GluRIID #	ATI.17 GluRIID #	1.36825E-24	***
WT.5 GluRIID #	ATI.33 GluRIID #	2.3473E-29	***
WT.5 GluRIIA intensity	ATI.5 GluRIIA intensity	0.008809949	**
WT.5 GluRIIA intensity	ATI.17 GluRIIA intensity	3.71503E-07	***
WT.5 GluRIIA intensity	ATI.33 GluRIIA intensity	0.048327587	*
WT.5 GluRIIB intensity	ATI.5 GluRIIB intensity	4.08533E-05	***
WT.5 GluRIIB intensity	ATI.17 GluRIIB intensity	1.00443E-07	***
WT.5 GluRIIB intensity	ATI.33 GluRIIB intensity	0.000222584	***
WT.5 GluRIID intensity	ATI.5 GluRIID intensity	0.91384072	N.S.
WT.5 GluRIID intensity	ATI.17 GluRIID intensity	0.001117841	**
WT.5 GluRIID intensity	ATI.33 GluRIID intensity	0.047545985	*
WT.5 mEPSP amplitude	ATI.5 mEPSP amplitude	0.327204201	N.S.
WT.5 mEPSP amplitude	ATI.17 mEPSP amplitude	4.01613E-05	***
WT.5 mEPSP amplitude	ATI.33 mEPSP amplitude	1.05448E-06	***
WT.5 mEPSP frequency	ATI.5 mEPSP frequency	0.397753778	N.S.
WT.5 mEPSP frequency	ATI.17 mEPSP frequency	0.000225276	***
WT.5 mEPSP frequency	ATI.33 mEPSP frequency	0.000437242	***
WT.5 decay Tau	ATI.5 decay Tau	0.9337	N.S.
WT.5 decay Tau	ATI.17 decay Tau	0.1614	N.S.
WT.5 decay Tau	ATI.33 decay Tau	0.0498	N.S.

Table S4. Data and statistical information. All absolute values (mean, SEM, N) and statistical information (tests used and P-values) for all data points shown in Fig. 4 are shown.

Symbol	Vesicle diameter nm (± SEM, N)
WT.5	29.88 (0.6789, 16)
ATI.5	28.71 (1.015, 16)
ATI.17	29.16 (0.3048, 17)
ATI.25	30.69 (1.598, 16)

Statistical Analysis: 1-way ANOVA with Tukey's multiple-comparison test

Array 1	Array 2	P-value	Symbol
WT.5 vesicle diameter	ATI.5 vesicle diameter	0.8455	N.S.
WT.5 vesicle diameter	ATI.17 vesicle diameter	0.9566	N.S.
WT.5 vesicle diameter	ATI.25 vesicle diameter	0.9408	N.S.

Table S5. Data and statistical information. All absolute values (mean, SEM, N) and statistical information (tests used and P-values) for all data points shown in Fig. 5 are shown.

Symbol	Quantal Content (± SEM, N)	Failures % (± SEM, N)	PPF EPSC1/2 % (± SEM, N)	PPD EPSC1/2 % (± SEM, N)
WT.5	32.02 (1.7, 11)	51.25 (6.09, 16)	149.91 (9.65,12)	74.35 (5.55, 11)
ATI.5	34.54 (1.62, 10)	61.39 (3.41, 9)	158.91 (13.97, 9)	81.34 (7.92, 8)
ATI.17	22.38 (1.55, 12)	79.17 (2.54, 12)	191.04 (11.11, 14)	96.76 (6.22, 14)
ATI.33	18.85 (1.43, 10)	76.73 (3.47, 13)	178.55 (10.86, 14)	102.09 (7.01, 13)

Statistical Analysis: 2-tailed Student's T-test

Array 1	Array 2	P-value	Symbol
WT.5 quantal content	ATI.5 quantal content	0.298373008	N.S.
WT.5 quantal content	ATI.17 quantal content	0.00026744	***
WT.5 quantal content	ATI.33 quantal content	1.18278E-05	***
WT.5 failures	ATI.5 failures	0.249077828	N.S.
WT.5 failures	ATI.17 failures	0.000840065	***
WT.5 failures	ATI.33 failures	0.002029811	**
WT.5 PPF	ATI.5 PPF	0.213347891	N.S.
WT.5 PPF	ATI.17 PPF	0.003167219	**
WT.5 PPF	ATI.33 PPF	0.006518763	**
WT.5 PPD	ATI.5 PPD	0.198726734	N.S.
WT.5 PPD	ATI.17 PPD	0.003167234	**
WT.5 PPD	ATI.33 PPD	0.002695262	**

Table S6. Data and statistical information. All absolute values (mean, SEM, N) and statistical information (tests used and P-values) for all data points shown in Fig. 6 are shown.

Symbol	Genotype	Time Point days AEL	Retractions (≥1 footprint) % NMJs (± SEM, N)	Boutons A4-M4-Ib # (± SEM, N)	BRP puncta # (± SEM, N)
WT.5	*w^{1118}*	5	8.33 (2.95, 9)		
ATI.5	*UAS-smox-RNAi/+; phm-Gal4/+*	5	4.69 (2.29, 8)	53.8 (7.05, 5)	358.53 (10.06, 15)
ATI.13	*UAS-smox-RNAi/+; phm-Gal4/+*	13	5.13 (2.51, 8)	74.71 (5.37, 7)	631.71 (26.27, 7)
ATI.17	*UAS-smox-RNAi/+; phm-Gal4/+*	17	6.55 (4.36, 6)		
ATI.21	*UAS-smox-RNAi/+; phm-Gal4/+*	21	6.94 (3.03, 9)		
ATI.33	*UAS-smox-RNAi/+; phm-Gal4/+*	33	10.42 (3.84, 6)		
stai.5	*$stai^{B200}$*	5	36.31 (8.58, 11)	9.13 (3.85, 8)	32.63 (11.3, 8)
stai.13	*$stai^{B200}$, UAS-smox-RNAi/$stai^{B200}$; phm-Gal4/+*	13	69.29 (5.02, 10)	16.63 (1.25, 8)	60.38 (13.26, 8)

Symbol	Genotype	Time Point days AEL	Footprints/ NMJ (A2) # (± SEM, N)	Footprints/ NMJ (A3) # (± SEM, N)	Footprints/ NMJ (A4) # (± SEM, N)	Footprints/ NMJ (A5) # (± SEM, N)
stai.5	*$stai^{B200}$*	5	0.14 (0.078, 21)	0.29 (0.14, 21)	1.09 (0.33, 22)	2.10 (0.52, 21)
stai.13	*$stai^{B200}$, UAS-smox-RNAi/$stai^{B200}$; phm-Gal4/+*	13	0.3 (0.18, 20)	1.5 (0.29, 20)	3.05 (0.59, 19)	5.65 (0.92, 20)

Statistical Analysis: 2-tailed Student's T-test

Array 1	Array 2	P-value	Symbol
stai.5 Retractions	stai.13 Retractions	0.001739115	**
ATI.5 A4 boutons	ATI.13 A4 boutons	0.036948124	*
stai.5 A4 boutons	stai.13 A4 boutons	0.08497713	N.S.
ATI.5 A4 BRP #	ATI.13 A4 BRP #	1.55159E-10	***
stai.5 A4 BRP #	stai.13 A4 BRP #	0.133588744	N.S.
stai.5 A2 footprints	stai.13 A2 footprints	0.418757225	N.S.
stai.5 A3 footprints	stai.13 A3 footprints	0.000400378	***
stai.5 A4 footprints	stai.13 A4 footprints	0.004994405	**
stai.5 A5 footprints	stai.13 A5 footprints	0.001560913	**

Table S7. Data and statistical information. All absolute values (mean, SEM, N) and statistical information (tests used and P-values) for all data points shown in Fig. S1 are shown.

	Baseline				+PhTx			
Symbol	**mEPSP Amp. mV (± SEM)**	**EPSP Amp. mV (± SEM)**	**Quantal Content (± SEM)**	**N**	**mEPSP Amp. mV (± SEM)**	**EPSP Amp. mV (± SEM)**	**Quantal Content (± SEM)**	**N**
WT.5	0.909 (0.038)	28.532 (1.166)	31.524 (1.275)	5	0.498 (0.017)	28.097 (0.93)	57.051 (3.442)	7
ATI.5	0.954 (0.062)	34.113 (1.928)	36.154 (2.263)	7	0.515 (0.019)	30.552 (1.184)	60.166 (4.105)	7
ATI.17	1.386 (0.108)	29.437 (0.81)	22.130 (2.005)	8	0.617 (0.022)	25.643 (0.763)	42.418 (1.791)	11
ATI.33	1.354 (0.077)	24.217 (0.905)	18.063 (0.688)	7	0.64 (0.03)	24.113 (1.363)	38.613 (2.820)	10

Statistical Analysis: 2-tailed Student's T-test

Array 1	Array 2	P-value	Symbol
WT.5 Baseline mEPSP	WT.5 +PhTx mEPSP	7.74747E-07	***
ATI.5 Baseline mEPSP	ATI.5 +PhTx mEPSP	4.8591E-06	***
ATI.17 Baseline mEPSP	ATI.17+PhTx mEPSP	4.21332E-07	***
ATI.33 Baseline mEPSP	ATI.33 +PhTx mEPSP	7.35985E-08	***
WT.5 Baseline EPSP	WT.5 +PhTx EPSP	0.774221103	N.S.
ATI.5 Baseline EPSP	ATI.5 +PhTx EPSP	0.133762953	N.S.
ATI.17 Baseline EPSP	ATI.17+PhTx EPSP	0.003103703	**
ATI.33 Baseline EPSP	ATI.33 +PhTx EPSP	0.956749384	N.S.
WT.5 Baseline Quantal Content	WT.5 +PhTx Quantal Content	0.000134197	***
ATI.5 Baseline Quantal Content	ATI.5 +PhTx Quantal Content	0.000217442	***
ATI.17 Baseline Quantal Content	ATI.17+PhTx Quantal Content	6.80559E-06	***
ATI.33 Baseline Quantal Content	ATI.33 +PhTx Quantal Content	4.42488E-05	***

Table S8: KEY RESOURCES TABLE

Antibodies			
REAGENT/RESOURCE	**SOURCE**	**IDENTIFIER**	**DILUTION**
Tetramethylrhodamine (TRITC)-conjugated phalloidin (R415)	Thermo Fisher Scientific	41-6559-05	1:1000
Mouse anti-Bruchpilot (nc82)	DSHB	AB_2314866	1:100
Guinea pig anti-vGlut	(Chen et al., 2017)	N/A	1:2000
Mouse anti-GluRIIA (8B4D2)	DSHB	AB_528269	1:50
Affinity-Purified Rabbit anti-GluRIIB	(Goel and Dickman, 2018)	N/A	1:2000
Guinea pig anti-GluRIID	(Kikuma et al., 2019)	N/A	1:1000
Rabbit anti-DLG	(Pielage et al., 2006)	N/A	1:10000
DyLight 405-conjugated secondary antibodies	Jackson ImmunoResearch Labs, Inc.	706-475-148	1:400
Alexa Fluor 488-conjugated secondary antibodies	Jackson ImmunoResearch Labs, Inc.	706-545-148, 715-545-150, 711-545-152	1:400
Cy3-conjugated secondary antibodies	Jackson ImmunoResearch Labs, Inc.	706-165-148, 715-165-150, 711-165-152	1:400
Alexa Fluor 647-conjugated Goat anti-Horseradish Peroxidase	Jackson ImmunoResearch Labs, Inc.	123-605-021	1:200
Experimental Models: Fly Lines			
REAGENT/RESOURCE	**REFERENCE**	**SOURCE**	
UAS-smox-RNAi	(Gibbens et al., 2011)	BDSC #41670	
phm-Gal4	(Ono et al., 2006)	BDSC #80577	
$stai^{B200}$	(Graf et al., 2011)	BDSC #16165	

Supplemental References:

Chen, X., Ma, W., Zhang, S., Paluch, J., Guo, W. and Dickman, D. K. (2017). The BLOC-1 Subunit Pallidin Facilitates Activity-Dependent Synaptic Vesicle Recycling. *eNeuro* **4**, ENEURO.0335-16.2017.

Gibbens, Y. Y., Warren, J. T., Gilbert, L. I., O'Connor, M. B., Cho, S. H., Smith, M. M., Padgett, R. W. and O'Connor, M. B. (2011). Neuroendocrine regulation of *Drosophila* metamorphosis requires TGFbeta/Activin signaling. *Development* **138**, 2693–2703.

Goel, P. and Dickman, D. (2018). Distinct homeostatic modulations stabilize reduced postsynaptic receptivity in response to presynpatic DLK signaling. *Nat. Commun.* **9**, 1856.

Graf, E. R., Heerssen, H. M., Wright, C. M., Davis, G. W. and DiAntonio, A. (2011). Stathmin is Required for Stability of the *Drosophila* Neuromuscular Junction. *J. Neurosci.* **31**, 15026–15034.

Kikuma, K., Li, X., Perry, S., Li Q., Goel, P., Chen, C., Kim, D., Stravropoulos, N. and Dickman, D. (2019). Cul3 and insomniac are required for rapid ubiquitination of postsynaptic targets and retrograde homeostatic signaling. *Nat. Commun.* **10**, 2998.

Ono, H., Rewitz, K. F., Shinoda, T., Itoyama, K., Petryk, A., Rybczynski, R., Jarcho, M., Warren, J. T., Marqués, G., Shimell, M. J., et al. (2006). Spook and Spookier code for stage-specific components of the ecdysone biosynthetic pathway in Diptera. *Dev. Biol.* **298**, 555–570.

Pielage, J., Fetter, R. D., and Davis, G. W. (2006). A postsynaptic spectrin scaffold defines active zone size, spacing, and efficacy at the *Drosophila* neuromuscular junction. *J. Cell Biol.* **175**, 491–503.